International Journal of Disaster Risk Reduction 128 (2025) 105736

Contents lists available at ScienceDirect

International Journal of Disaster Risk Reduction

journal homepage: www.elsevier.com/locate/ijdrr

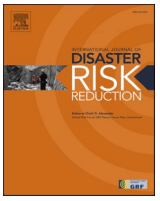

# Cascading impacts of individual failures across critical infrastructures: The case of upper dam breach in pumped-storage hydropower schemes

Panagiotis Dimas [a,*], Archontia Lykou [a], Akis Zarkadoulas [a], Georgia-Konstantina Sakki [a], Andreas Efstratiadis [a], Christos Makropoulos [a], Argyro Louloudi [b]

[a] Department of Water Resources and Environmental Engineering, School of Civil Engineering, National Technical University of Athens (NTUA), 15780, Athens, Greece
[b] Environmental Licensing Unit, Hellenic Public Power Corporation (PPC S.A.), Athens, Greece

ARTICLE INFO

*Keywords:*
Pumped-storage hydropower systems
Dam failure mechanisms
HEC-RAS
BASEbreach
Impulse wave generation

ABSTRACT

The assessment of critical infrastructures vulnerable to cascade failure phenomena requires a holistic viewpoint accounting for the full cause-effect chain. A key case is the upper dam failure in pumped-storage hydropower (PSH) systems, which can severely impact downstream infrastructures. This study proposes a generalized framework to examine the potential consequences of this catastrophic event, which is then showcased to a planned pumped-storage system in the Aliakmon River basin, Greece. It integrates hydrodynamic simulations and semi-empirical approaches to assess dam failure mechanisms and flood wave propagation, impulse wave generation, flood routing through the lower reservoir, and resulting risks. Several scenarios are deployed through HEC-RAS and BASEbreach models, accounting for the influence of terrain on wave dynamics and flood propagation. Impulse waves generated by sudden water inflows are modeled using theoretical and semi-empirical methods, with key parameters such as wave amplitude, run-up, and attenuation evaluated under both 2D and 3D propagation conditions. The core scientific question is whether wave heights and run-up remain within safety thresholds, and how resilient PSH systems are under cascading failures. The framework supports enhanced risk assessment, resilient hydropower design, and sustainable water-energy infrastructure planning.

## 1. Introduction

The term “critical infrastructure” is applied to systems, facilities and assets that are vital for the functioning of society and the economy. Often, these comprise several interconnected components, whose local-scale malfunction or damage may cause adverse impacts to the entire system, by means of cascade failure phenomena. In this vein, the resilience of critical infrastructures should be addressed from a holistic viewpoint, thus emphasizing to complex effects of individual failures and interplays among the associated system components.

A typical case involves individual failure effects across pumped storage hydropower (PSH) systems [1]. The expanding

* Corresponding author.
*E-mail address:* pdimas@mail.ntua.gr (P. Dimas).

https://doi.org/10.1016/j.ijdrr.2025.105736
Received 28 March 2025; Received in revised form 28 July 2025; Accepted 29 July 2025
Available online 2 August 2025

development of these critical infrastructures [2,3], which are pivotal in balancing energy grids and integrating renewable energy sources [4–6], has highlighted the emerging need to address the risks associated with dam breaks [7–11]. These facilities, typically composed of two interconnected reservoirs, operate by lifting water from the lower to the higher reservoir, and vice versa, to store and release energy, respectively [12–15]. However, the proximity of reservoirs, coupled with their operational dynamics, introduces unique challenges in managing cascading effects during upper dam failure events [11,16–18]. Such risks are amplified in mountainous terrains where the rapid transfer of water and the confined topography can exacerbate downstream hazards [19–25].

Dam-break events are inherently probabilistic, driven by a complex interplay of natural and anthropogenic factors, including extreme precipitation [26], seismic activity, operational failures, and structural defects [27]; [28]; [29]; [30–32]. For upper reservoirs, the risk of failure is compounded by their elevation and stored potential energy [33–35]. When breached, these can unleash massive volumes of water to downstream systems, leading to rapid inundation and secondary disasters, such as landslide-induced surges and tsunami-like waves in the lower reservoir [36–41]; [42]. These dynamic phenomena underscore the need for comprehensive probabilistic risk assessments and hydrodynamic modeling to anticipate and mitigate their impacts [30,43–46].

The hydrologic response of the lower reservoir to an upper dam break is multifaceted, since the sudden influx of water not only alters the storage dynamics but also modifies the morphological and hydrodynamic conditions of the downstream system. Key processes include flood wave propagation, amplification of flow velocities, and the generation of tsunamis as the incoming water interacts with the reservoir's surface, mimicking a landslide-induced impulse wave [47–50]. These phenomena create dual challenges: accurately modeling the breach dynamics and understanding the downstream hydrodynamic response to optimize emergency response strategies and infrastructure resilience [15,51–53].

Numerical simulations and physical models provide valuable insights to these processes, enabling the prediction of breach evolution, flood wave routing, and inundation patterns [54–58]. Tools like the DB-IWHR model [59–61], the HEC-RAS dam break module [62–66], and two-dimensional shallow water flow simulations have demonstrated their efficacy in capturing the temporal and spatial characteristics of dam-break events under varying conditions [67–72]. For example, several studies have shown how breach formation parameters, such as breach side slope, material erodibility, etc., govern the discharge hydrograph, while downstream flood routing is influenced by the river morphology and the reservoir operating levels [73], i.e. initial levels at the breaching initiation [74–78].

Despite these advancements, the cascading effects of dam breaks across PSH schemes remain underexplored. Unlike conventional systems, these configurations introduce dynamic interdependencies where upper dam breaches may rapidly compromise downstream components, potentially causing impulse waves and overtopping. Addressing this gap, the present study develops and demonstrates a comprehensive modeling framework that integrates multiple methods to capture the complexity of such cascading events. The faithful representation of the entire chain requires detailed simulations that incorporate coupled breach models, multi-scale hydrodynamic analysis and outflow structures routing [79–82]; [83]. Furthermore, the decisions regarding the management of the flood entering the lower reservoir, namely spillway gate opening and hydropower station operation, may be subject to external constraints from the electricity grid perspective. The key scientific questions are: *(a)* how can cascading failures in PSH schemes be systematically modeled under uncertainty? and *(b)* what thresholds ensure resilience against overtopping or sequential dam failures? Answering these informs both academic understanding and practical design.

This study centers on the PSH system associated with the Sfikia reservoir, situated in Aliakmon River basin, Northern Greece, which is part of a network of interconnected hydroelectric reservoirs in series. The project encompasses the connection of the existing reservoir with a proposed upper reservoir at Brava via the essential hydraulic infrastructure. Using a combination of advanced simulation techniques and empirical methods, this research investigates the potential failure mechanisms of the upper dam, with a particular focus on piping failures [84,85], and examines how such events influence flood wave dynamics as they propagate downstream, toward the Sfikia dam. Multiple failure scenarios are explored, employing hydrodynamic simulations to analyze flood wave propagation and assess the downstream impacts. Emphasis is placed on understanding the hydrologic routing of the flood hydrograph and the generation of large-scale impulse waves resembling tsunami phenomena. The findings aim to inform the development of risk mitigation strategies [15], including warning systems and preventative measures, to enhance the safety and resilience of the integrated pumped-storage hydropower system [86,87].

While several studies -as analyzed before-have addressed dam-break dynamics and emergency planning for single-reservoir systems or sequential cascades [88], pumped-storage hydropower (PSH) schemes present unique modeling challenges due to their bidirectional operation, close reservoir proximity, and potential for rapid cascading effects. The literature has yet to fully integrate breach modeling, flood propagation, impulse wave generation, and operational constraints into a unified framework tailored for PSH settings. This study addresses that gap by synthesizing a plethora of tools into a reproducible methodology that supports both technical planning and resilience assessment.

## 2. Methodological framework

### 2.1. Overview

The assessment of cascading effects in pumped-storage hydropower schemes requires an integrated modelling framework that consists of five key components: (i) dam breach simulation; (ii) flood wave propagation analysis; (iii) flood hydrograph routing across the reservoir(s) composing the greater scheme, (iv) impulse wave (tsunami) generation and propagation, and (v) an overarching uncertainty-aware approach.

The diagram of Fig. 1 illustrates the chain of process and associated modelling elements for assessing the cascading effects of dam failure within a PSH scheme. It highlights the interaction between hydrologic inflows, dam breaches, and subsequent risks to

downstream infrastructures. The generic process begins with a flood inflow entering the upper reservoir, which, in the event of a dam failure, generates a hydrograph that propagates downstream as a flood wave. This is routed into the lower reservoir, which may also receive additional inflows, both natural (i.e., flood from upstream basins) and regulated (i.e., from turbines, spillways, and other hydraulic works). The subsequent hydrologic routing and impulse wave generation (tsunami-like effects) may significantly influence the water balance dynamics of the lower reservoir, up to posing a risk of overtopping its dam. Simultaneously, the lower reservoir releases water through turbines and spillways, thus transferring the effects further downstream to additional reservoirs or hydraulic structures. Each downstream infrastructure component is evaluated for the risk of overtopping, ensuring a systematic assessment of cascading failure scenarios. The diagram also dictates several physical and modeling uncertainties, acknowledging the complexities in predicting flood wave behavior, hydrologic routing, and dam stability. This framework provides a structured approach for assessing the interdependencies of reservoirs in a pumped-storage system and identifying potential failure mechanisms that could lead to widespread risk.

To handle the modeling uncertainties inherent in dam breach analysis and wave propagation, we adopted a scenario-based approach. Multiple different breach simulations, using diverse models with varying assumptions, are conducted to explore a plausible range of outcomes. This approach provides a structured yet practical alternative to fully probabilistic modeling.

### 2.2. Dam breach simulation

Dam failure can happen due to a multitude of mechanisms, such as extreme flood event, piping/seepage, landslide, earthquake, foundation failure, equipment failure/malfunction, structural failure, upstream dam failure, rapid drawdown of pool, sabotage [89], and planned removal [90]. The dominant failure reasons of embankment dams are overtopping and piping [91,92].

An overtopping failure occurs when the water level in a reservoir exceeds the dam crest, leading to uncontrolled flow over the structure. The process can either be initiated by extreme hydrologic inflows from the upstream basin due to a heavy storm event (flooding), often combined with inadequate spillway capacity, or by operational malpractices/mismanagement. For instance, the optimal control of gated spillways is subject to increased risk of overtopping, particularly when the operator must take decisions under highly stressed and highly uncertain conditions [93]. In the case of PSH systems, which is the focus of this research, an overtopping may also be due to malfunctions of the electromechanical machinery and associated control devices. A characteristic example is the 2005 upper Taum Sauk Dam overtopping, due to the failure of reservoir stage sensors that led to over-pumping from the lower reservoir [94,95]. Nevertheless, overtopping erodes the dam's downstream face, progressively weakening its integrity and eventually causing structural collapse (Fig. 2). Unlike internal erosion (piping), which develops gradually, overtopping failure can lead to rapid and catastrophic breach formation. The severity of failure depends on factors such as dam material, water velocity, and erosion resistance. Earthen dams are particularly vulnerable, as the flowing water quickly erodes the embankment, accelerating failure.

Internal erosion, usually referred to as piping, occurs when localized leaks develop within the dam body or its foundation. This

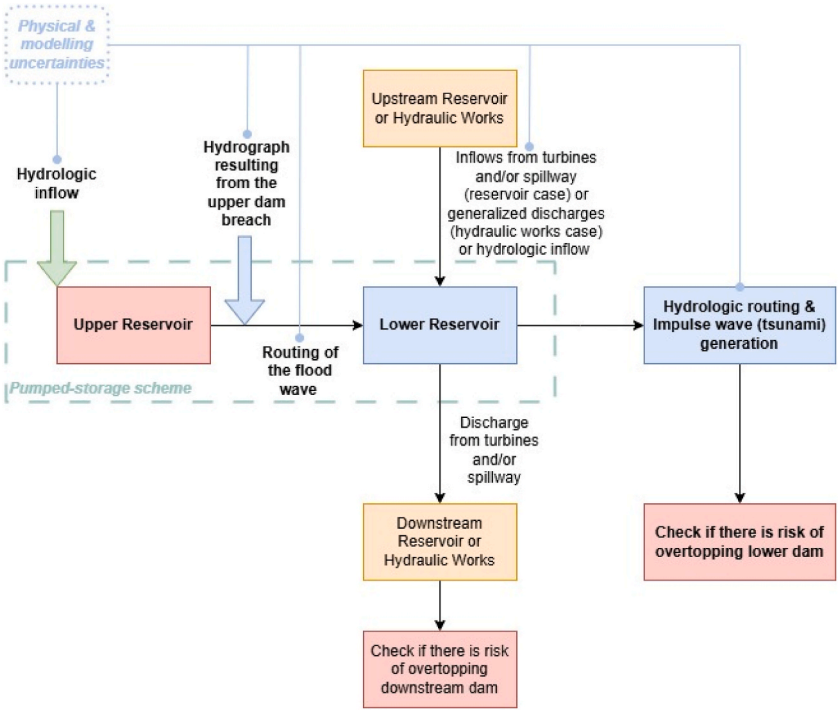


**Fig. 1.** Outline of the generalized methodological framework.

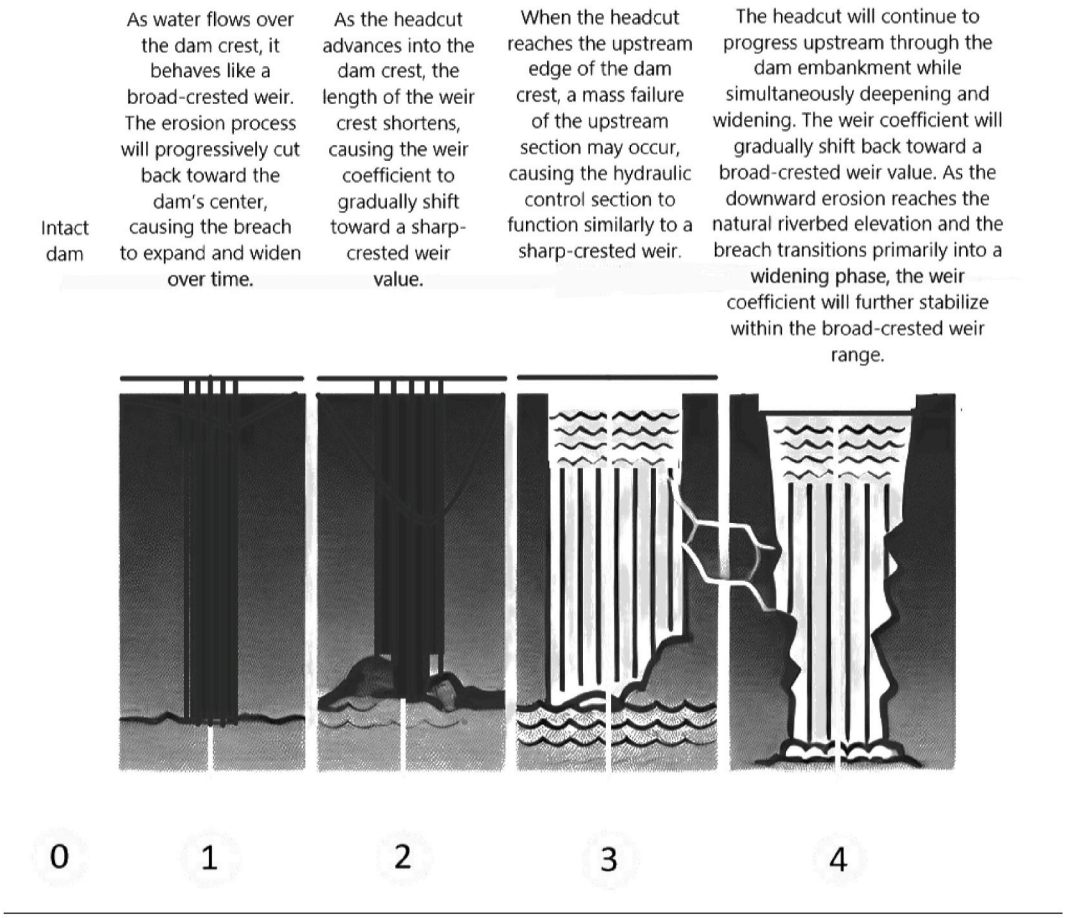


**Fig. 2.** Progression of failure event due to overtopping: (a) in a front view of the dam (Inspired by: [90]), (b) in a perspective view (Inspired by: [96]).

phenomenon can result from compaction failures or differential settlements, particularly when technical specifications for dam construction are not adequately followed. Fig. 3 illustrates the progression of a failure process in an earthen dam caused by internal erosion.

The key parameters for modeling dam failure mechanisms are related to the geometric characteristics of the breach, including the

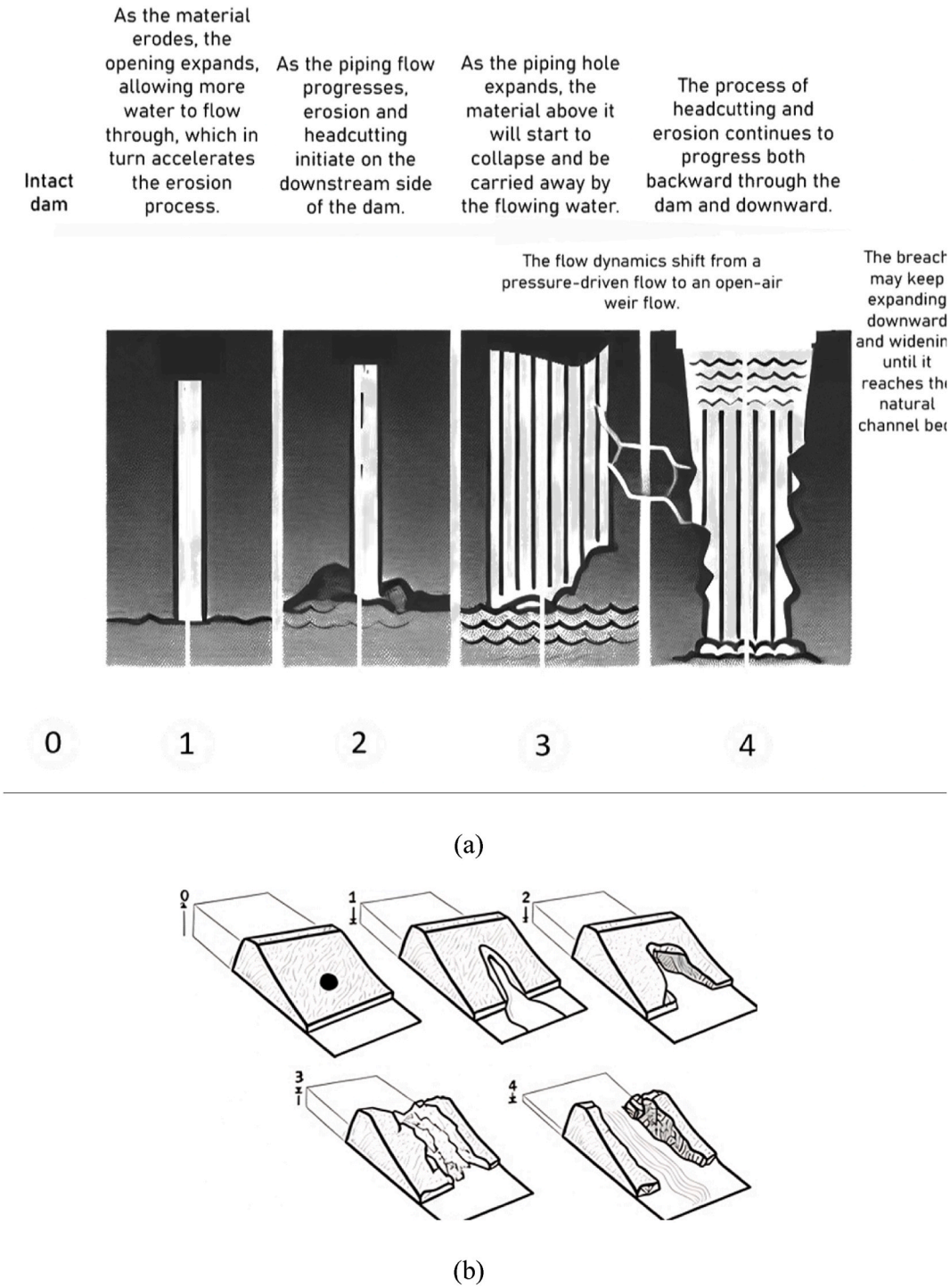


**Fig. 3.** Progression of failure event due to piping: (a) in a front view of the dam (Inspired by: [90]), (b) in a perspective view (Source: [96]).

average breach width, $B_{ave}$, the bottom breach width, $W_b$, the breach height, $h_b$, and the water depth, as measured from the bottom to the maximum level of the free surface, $h_w$.

The HEC-RAS software is mostly used to represent the evolution of a dam breach. This incorporates regression equations derived from observed data of historical dam failures and allows for the input of erosion parameters to simulate simplified breach processes. The HEC-RAS embeds alternative models, namely by Froehlich (1995)[97], Froehlich [98], MacDonald and Langridge-Monopolis [99], Von Thun and Gillette [100], and Xu and Zhang [101]. Detailed information about each equation set can be found in the

documentation document [90], which also provides guidance on model selection. A general recommendation is the use of multiple equation sets to generate a range of parameter values and evaluate the resulting hydrographs.

Another well-known software is the so-called BASEbreach [102,103], including three methods, i.e. Macchione [104], Peter [105] and Peter calibrated. Detailed information is provided in the documentation report (https://gitlab.ethz.ch/vaw/public/basebreach/-/wikis/dam-breach-models).

### 2.3. Hydrodynamic modelling

The generalized framework incorporates hydrodynamic modeling to simulate the flood routing between the upstream and downstream storage components of the PHS scheme, namely the breached upper reservoir and the lower one. This model should rely on a high-resolution Digital Terrain Model (DTM). The two-dimensional flow area can be developed within the HEC-RAS environment [106], or any other capable hydrodynamic model, to capture the region of interest (i.e., river course and floodplains) downstream of the upper dam up to the banks of the lower reservoir.

Key requirements are: (a) building a computational grid of proper spatial discretization comprised by finite volume cells of size $\Delta x$, to ensure numerical stability without refinement in high-slope areas; (b) choosing a proper time step, $\Delta t$, to satisfy the Courant-Friedrichs-Lewy (CFL) criterion, i.e., $CFL = \frac{u \cdot \Delta t}{\Delta x} \leq 1$ [107]; and (c) adopting a proper Manning roughness coefficient for the channel and floodplain areas [108].

The boundary conditions [109] to be defined are: (a) the scenario-specific outflow hydrographs, as produced by the dam breaching modeling approach; and (b) a stage-time curve at the downstream boundary, with a constant stage set to the Maximum Operating Level (MOL) of the lower reservoir throughout the flood event.

### 2.4. Routing of the flood hydrograph through the lower reservoir

The propagation of the flood hydrograph entering the lower reservoirs is subject to the presence of spillways, gates and other outflow control structures (e.g., turbines), which allow for partial or full attenuation of the incoming wave. Even in the worst-case scenario of a full reservoir at the arrival time of the flood wave, the latter will be temporarily stored and routed to the downstream system with a longer base time and reduced peak flow.

Input data of the routing model are the inflow hydrograph, $i_t$, the stage-storage relationship of the reservoir, $s = s(z)$, the stage-discharge relationship of the spillway and the rest of outflow structures, $q = q(z)$, and the initial reservoir level, $z_0$. Outputs are the outflow hydrograph, $q(t)$, and the time evolution of the reservoir level, $z(t)$. The routing problem is based on the water balance equation:

$$ds / dt = i(t) - q(t) \tag{1}$$

which is written in a discrete form as:

$$s(z_j) - s(z_{j-1}) = \frac{1}{2} \left[ i_j + i_{j-1} - q(z_j) - q(z_{j-1}) \right] \Delta t \tag{2}$$

At each time step $j$, terms $s(z_{j-1})$, $q(z_{j-1})$, $i_j$, and $i_{j-1}$ are known, while $s(z_j)$ and $q(z_j)$ are nonlinear functions of $z_j$. The water balance formula can be solved either iteratively or as a system of nonlinear equations, if setting the initial condition $z_0$ at $t_0$, and expressing $s(z)$ and $q(z)$ via appropriate analytical formulae.

The stage-storage relationship may be expressed as a power function of the form:

$$s(z) = \kappa (z - z_b)^{\lambda} \tag{3}$$

where $z_b$ is a characteristic low elevation (datum), such as the elevation of the bed at the dam site, and $\kappa$, $\lambda$ are scale and shape parameters, respectively, that can be estimated through regression analysis of the reservoir's geomorphology [110].

The stage-discharge relationship of the spillway depends on whether this is free or gated. In the first case, the hydraulic formula is written as [111]:

$$q = c \sqrt{2g}\, W_e\, H^{3/2} \tag{4}$$

where $c$ is a discharge coefficient, depending on the flow conditions and the geometry of the ogee, $W_e$ is the effective width of the spillway (total length, $W$, reduced to account for minor hydraulic losses), and $H$ is the hydraulic head, defined as the flow depth above the crest, $z - z_c$, and the kinetic energy term. In fact, eq. (4) is quite complex, since both $c$ and $H$ are functions of the outflow discharge, $q$. In this respect, in several practical applications, eq. (4) is simplified by handling term $C = c\sqrt{2g}$ as a constant, by setting the full width instead of the effective one, and by omitting the kinetic energy term, i.e.:

$$q = C\, W\, (z - z_c)^{3/2} \tag{5}$$

In the case of large outflow conditions, it is recommended to slightly increase the shape parameter 3/2, as a proxy of accounting for the kinetic energy term. Recent research by Efstratiadis [112] demonstrated that using the flow depth and adjusting the exponent achieves

results equivalent to the more precise yet computationally complex approach that includes the kinetic energy term.

In the case of gated spillways (which are generally applicable in hydropower dams), the outflow dynamics are also subject to the restriction/choking effect of the sluice gates. The representation of the submerged flow under gates is extremely complex, thus in practical problems, simplified empirical approaches are strongly preferred. A widely used expression to account for the influence of gates when the flow approaches their downstream face is proposed by the HEC-RAS Hydraulic Reference Manual [113], and approximates the outflow $q$ as follows:

$$q = c\sqrt{2g}\, W\, T^{TE} B^{BE} H^{HE} \tag{6}$$

where $c$ the discharge coefficient (typical range from 0.6 to 0.8), $W$ the width of the gated spillway, $T$ the trunnion height (from spillway crest to trunnion pivot point), $TE$ an exponent factor (typically value 0.16, default 0.0), $B$ the height of the gate opening, $BE$ an exponent factor, (typical value 0.72, default 1.0), and $H$ the upstream energy head above the spillway crest.

The routing problem may also be subject to additional processes, such as inflows from the upstream system and controlled outflows from other hydraulic structures, as well as operational constraints, regarding hydropower scheduling, gate opening, etc., that must be represented in the mathematical framework. Eventually, the total outflow passing from the lower reservoir may be input of a more extended simulation chain, to assess cascade effects across the downstream system.

### 2.5. Impulse wave (tsunami) generation modeling

#### 2.5.1. Problem setting and assumptions

Impulse waves, widely known as tsunamis, are generated when abrupt disturbances occur at the boundaries of a water body, such as a sudden influx of water or landslides. These waves differ depending on the source. Surface landslides create disturbances with wavelengths comparable to their heights, as opposed to submarine landslides, which typically produce tsunami waves with longer wavelengths relative to their height. In the proposed framework, the sudden entry of a large portion (or even the entire quantity) of the water stored in the upper reservoir into the lower reservoir is treated analogously to a surface landslide, namely a concentrated mass falling into the lake and propagating as an impulse wave. In this vein, the key question is whether this tsunami will set the dam safety under risk, in the case of overtopping.

In the proposed framework, two alternative options are recommended, the first one based on an analytical yet simplified representation of the wave processes, and the second one employing a more detailed semi-empirical approach.

#### 2.5.2. Theoretical approach

The theoretical model used to simulate impulse wave generation is based on the pioneering work of Sir Scott Russell [114] and subsequent advancements by Di Risio and Sammarco [115]. It represents the wave generation mechanism as a vertical mass (or "box") falling into a 2D water body initially at rest. The phenomenon is divided into two main phases, i.e.: (a) impact phase, where the box strikes the water's free surface, transferring energy to the fluid as impulse pressure, and (b) submersion phase, where the box continues to submerge until reaching the bottom, affecting wave propagation characteristics.

The analytical description of this process accounts for both pressure impulses, $P = \rho_s d\Delta V$, where $\rho_s$ is the mass density and $\Delta V$ its velocity, and velocity distributions. The wave height $n(x,t)$ generated by the disturbance is given by:

$$n(x,t) = 2\frac{P}{\rho\beta(t)}\sqrt{\frac{h}{g}}\left\{A_i[Z(x+L,t)] - A_i\left[Z(x+L,t)+\frac{L}{\beta(t)}\right]\right\} + \int_0^{t_{im}} \frac{LV(\tau)}{\beta(t-\tau)} A_i[Z(x,t-\tau)]d\tau$$
$$+\frac{P}{\rho}\int_0^t \frac{1}{\beta(\tau)}\frac{1}{\beta(t-\tau)} A_i[Z(x,t-\tau)]\{A_i[Z(2L,\tau)] + A_i[Z(0,\tau)]\}d\tau \tag{7}$$

where $\beta(t) = \left(\frac{1}{2}\sqrt{gh}\,h^2 t\right)^{1/3}$, $Z(x,t) = \frac{x-\sqrt{ght}}{\beta(t)}$, $A_i$ is the so-called Airy function [116], and $t_{im}$ is the time interval for the box to come to rest after its initial impact.

Although the interaction between the mass and the water is highly complex, simplifications are made to focus on predicting wave characteristics far from the source. This approach offers two main benefits, since it is conservative (provides a first-order prediction of maximum wave height, neglecting energy dispersion), and may also serve as an analytical benchmark for validating numerical models.

Additional factors that further diminish the impulse wave amplitude are the attenuation of the wave, the radial spreading and the diffraction effects. In particular, the wave energy dissipates due to bottom friction, which is particularly significant in shallow water. The friction factor, $f_w$, depends on the Reynolds number and bed roughness and can be modeled through the empirical relationships (e.g. Ref. [117]):

$$f_w = 0.237 r^{-0.52}, r = \frac{A}{k_s}, A = u_m T \Big/ 2\pi \tag{8}$$

where $u_m$ is the maximum near-bed velocity, and $k_s$ is the grain size or roughness length.

Furthermore, the wave height diminishes as the wave spreads radially. The decay is governed by exponential relationships derived from wave energy conservation laws, as shown in Evers et al. [25]. Finally, near obstacles, diffraction alters wave propagation patterns.

The Helmholtz equation is often used to model wave diffraction, particularly around semi-infinite barriers [118].

#### 2.5.3. Semi-empirical approach

Estimating and analyzing the impulse waves effects through the semi-empirical approach is based on a suite of recent tools developed by the Laboratory of Hydraulics, Hydrology, and Glaciology (VAW) at ETH Zürich [25]. The underlying methodology provides practical, generally applicable equations for estimating wave characteristics and their impacts on dam infrastructure, across two phases, i.e.: (a) wave generation and propagation; and (b) wave run-up and overtopping.

Regarding phase (a), the wave characteristics, including amplitude, height, and attenuation, are determined using empirical equations. The analysis distinguishes between 2D propagation (longitudinally confined wave movement) and 3D propagation (radial free wave spreading). 3D spreading dissipates energy faster, resulting in smaller wave heights compared to 2D scenarios. Key inputs include the slide impact velocity, $V_s$, volume, $\bar{V}_s$, and thickness, $s$, the reservoir width, $b$, the still water depth, $h$ and the slide density, $\rho_s$. Equations for estimating wave amplitude (e.g. $\alpha_{c1}$, $\alpha_{t1}$) account for these variables and reservoir geometry, as illustrated in Figs. 4 and 5.

The methodology also evaluates wave run-up at critical locations, such as the dam site and opposing reservoir shores, by employing 2D analyses. The charsacteristic quantities affecting run-up include the wave height near the dam, $H$, the still water depth, $h$, the slope angle of the dam face, $\beta$, and the freeboard height, $f$. The run-up height is then calculated by using the empirical relationship (with $\alpha$ being the wave amplitude right before the run-up):

$$R = 2\,a\,exp(0.4\varepsilon)\left(\frac{90^0}{\beta}\right)^{0.20},\ \varepsilon = \alpha \Big/ h \tag{9}$$

## 3. Study area

### 3.1. System layout and problem setting

Cascading hydropower reservoir systems optimize river hydrodynamics while reducing flood risks in downstream regions, thus offering greater flexibility compared to standalone projects [119]. The Aliakmon River Complex in Greece exemplifies this configuration, since it involves four large hydroelectric reservoirs is series (Ilarionas, Polyfyto, Sfikia, Asomata), regulated downstream by a smaller one (Agia Varvara). Sfikia and Asomata also form an open-loop PSH scheme across the complex, which is one of the two large-scale pumped-storage works in Greece. The operator of the reservoirs is the Public Power Corporation (PPC S.A.).

The Brava-Sfikia pumped-storage system is a recently proposed project, whose design is still in preliminary phase. This aims at utilizing the existing Sfikia reservoir as the lower reservoir and connecting it with an upper reservoir to be created on a neighboring plateau at the location "Brava" (approximately 0.6 km southeast of the lake). While Sfikia integrates with the broader Aliakmon complex, receiving inflows from Polyfyto and discharging into Asomata, the Brava reservoir will form a practically closed PSH system, with negligible natural inflows.

This study aims to evaluate the cascading impacts of potential Brava dam failures on the Sfikia reservoir and the downstream infrastructure. Central questions include identifying failure mechanisms, modeling critical parameters under uncertainty, assessing flood wave propagation, and analyzing adverse effects, due to technical and operational constraints as well as additional stresses from the upstream system (by means of outflows from Polyfyto). A key focus is the assessment of the likelihood of Sfikia dam overtopping and subsequent cascading effects downstream. To address these challenges, the generic framework presented in Section 2 is applied, emphasizing at potential failure mechanisms of Brava dam and flood hydrograph generation, hydraulic routing of the flood wave to Sfikia, and impacts on Sfikia under various operational scenarios and impulse wave (tsunami) generation. These insights aim to enhance risk mitigation and ensure the resilience of the interconnected hydropower system.

The study area (see Fig. 6) focuses on the hydrographic network and the region between the proposed upper reservoir at Brava, developed as part of the pumped-storage project, and the existing lower reservoir, which is the Sfikia reservoir. Key infrastructures relevant to this study include the upper and lower dams and reservoirs, i.e. Brava and Sfikia, respectively, along with their auxiliary works, the key technical characteristics of which are briefly presented in the next section. The upstream Polyfyto reservoir will also be

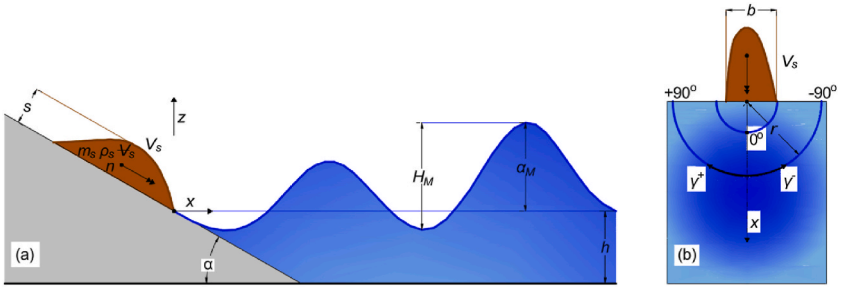


**Fig. 4.** (a) Illustration of main mechanisms of wave generation for the 2D case and (b) corresponding coordinate system (Source: [25]).

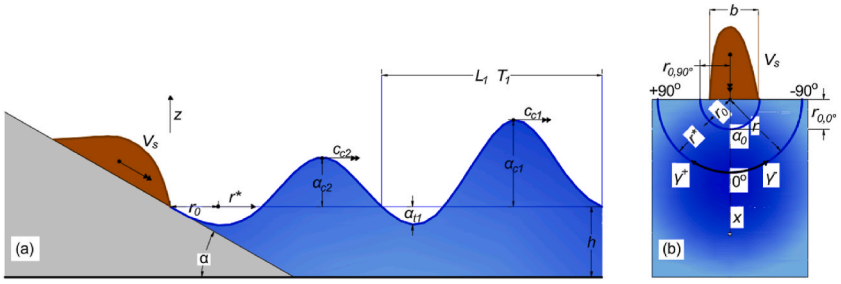


**Fig. 5.** (a) Illustration of main mechanisms of wave generation for the 3D case and (b) corresponding coordinate system (Source: [25]).

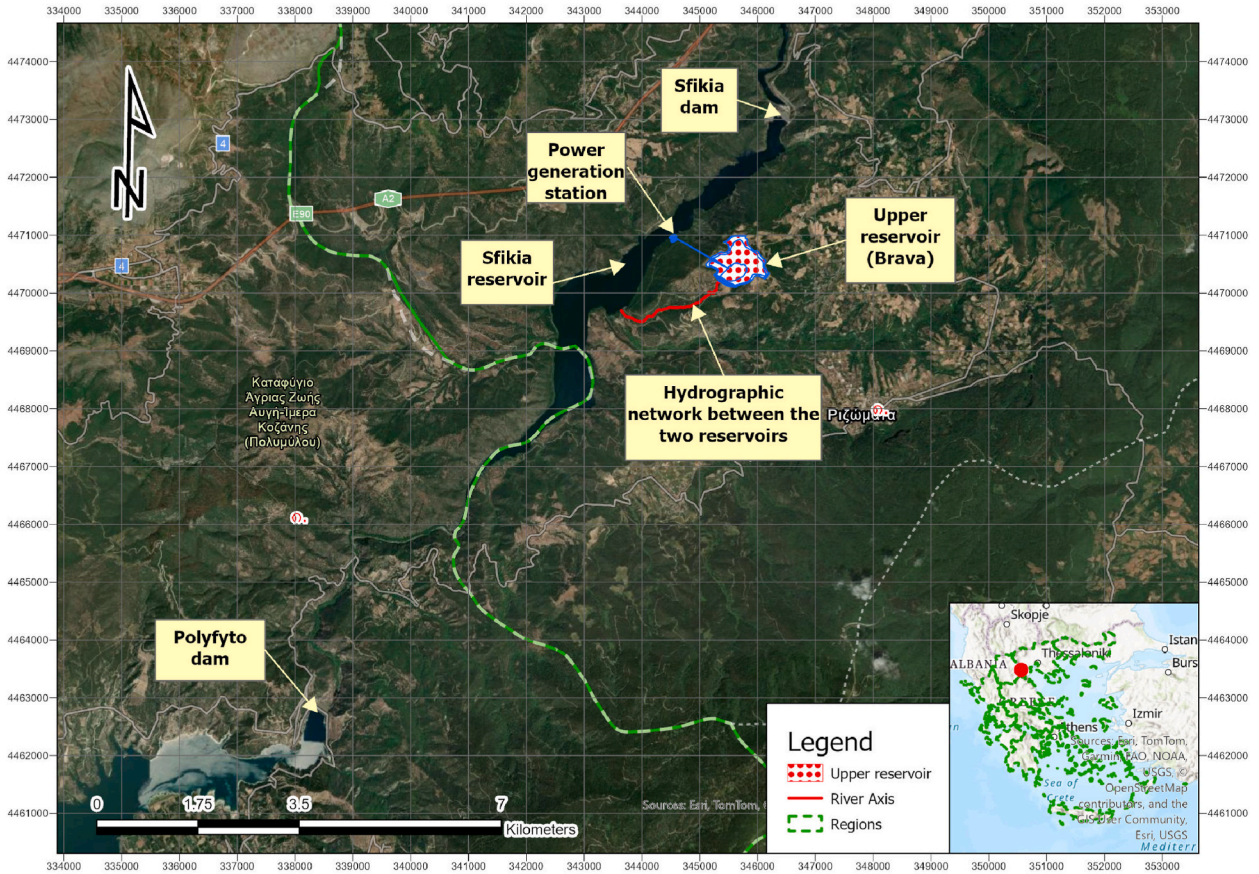


**Fig. 6.** Study area and location of the upper reservoir (Brava) of the pumped-storage scheme in relation to the Sfikia reservoir, which serves as the project's lower reservoir (Basemap source: ESRI et al., 2025).

accounted for in the analysis, by means of additional inflows to Sfikia reservoir, originating from its turbines and its spillway.

### *3.2. Technical data*

#### *3.2.1. Description of pumped-storage scheme*

Key components of the PSH scheme are one main and two auxiliary dams allowing to formulate the upper reservoir at Brava plateau, a reverse hydropower station, to be sited on the southeast shore of Sfikia reservoir, and an underground pipeline system connecting the upper reservoir intake to the station. The power capacity of the system will be 441 MW for hydroelectric production and 467 MW for pumping.

The upper reservoir is designed to take advantage of the favorable morphology of the area to be inundated. In this vein, a 435 m long, 45 m high earth dam is proposed to be constructed at the southwest edge of the basin, supported by two smaller auxiliary dams. The maximum operational level will be +560.0 m, corresponding to a maximum lake area of 0.54 $km^2$ (the total area of the

surrounding basin is 0.79 km$^2$), and a total storage capacity of 10.25 hm$^3$. For the pumped storage schedule, two operational modes are foreseen, namely intraday (8 h production, 11 h pumping) and a more extended one (21 h production, 29 h pumping). The first mode will require an active storage volume to recycle equal to 3.80 hm$^3$, and the second one 9.96 hm$^3$. The reservoir levels (minimum operation levels) at the end of each production phase will be +552.3 m + 530.0 m, respectively.

#### 3.2.2. Lower reservoir (Sfikia) characteristics

The Sfikia Hydroelectric Power Plant (HPP) is located on the middle course of Aliakmon, which is the longest river spanning exclusively in the Greek territory. Its main components include a rockfill dam of 82 m height, formatting a reservoir of total storage capacity of 100 hm$^3$ (active capacity 18 hm$^3$). The minimum and maximum operational levels are +141.8 and + 146.0 m, the maximum flood level is +147.0 m, and the dam crest is at +150.7 m. Additional structures include two gated spillway tunnels, of maximum discharge capacity of 1600 m$^3$/s, three intake tunnels of 160 m length, and an underground powerhouse equipped with three vertical-axis reversible Francis turbines, each with a capacity of 105 MW (total capacity 315 MW). Its construction began in 1979, and the station became operational between 1985 and 1986.

Sfikia is the first hydropower station in Greece equipped with reversible units, capable of functioning both as generators and pumps. During periods of low electricity demand or low electricity market prices, the station pumps water from the downstream Asomata reservoir, while it generates peak electricity during peak demand periods. The average annual energy production is estimated at 380 GWh, of which 200 GWh is generated through pumped storage. This feature underscores the significance of the plant as a cornerstone of Greece's energy storage landscape.

The flood discharge system at Sfikia is located on the left abutment, near the power station, and consists of two parallel tunnels with a diameter of 7.5 m. Upstream flow is controlled by four gates, each 7.2 m wide and 9.0 m high. Both tunnels include a steep upstream section and a milder downstream one, ending with a chute structure. The crest of the flow control structure (ogee) is at +137.0 m. The system is designed exclusively for free-surface flow conditions.

## 4. Analysis of upper dam breach processes

### 4.1. The case of overtopping

A first question to address is whether the Brava dam is possible to fail due to a flood inflow causing overtopping. Given the small extent of the surrounding basin, i.e. 0.79 km$^2$, a conservative approach is employed, by investigating three flood events generated by an extreme rainfall event of 10,000 years return period. Three rainfall durations are considered, i.e. (a) 10 min, thus equal to the basin's time of concentration; (b) 24 h, which is a typical design duration for flood protection infrastructures across small basins; and (c) 72 h, to account for prolonged extreme rainfall events, similar to the recent (September 2023) catastrophic Medicane "Daniel" [120].

For the estimation of the 10,000-years rainfall, the updated Intensity-Duration-Frequency curves are utilized. These were developed as part of the first revision of the National Flood Risk Management Plans [121]. For the estimation of the flood volume, we consider the effective rainfall falling over the net basin area, i.e. 0.25 km$^2$, and the rainfall falling over the lake area, i.e. 0.54 km$^2$. The effective rainfall is estimated via the well-known runoff curve number method, by setting $CN = 70$ and assuming an initial abstraction ration equal to 20 %. The results are presented in Table 1.

The resulting flood volumes are compared to the available buffer volume from the Maximum Operating Level (+560 m) to the crest elevation (+561 m), which is estimated up to 620,000 m$^3$. Even under the unfavorable combination of the worst-case inflow scenario (flood volume ~ 480,000 m$^3$) that finds the reservoir at its MOL, and simultaneous non-operation of the turbines and bottom outlets (conservative hypothesis), the flood volume is clearly smaller than the available buffer. Consequently, the overtopping scenario is not further considered as a potential dam breach mechanism.

### 4.2. Investigation of dam breach due to piping

#### 4.2.1. Configuration of piping scenarios

The case of dam breach due to piping is investigated following the rationale of section 2.2. Given that the phenomenon is highly uncertain, ten scenarios are configured that are summarized in Table 2. These make use of the five available equation sets included in HEC-RAS. Particularly, for the Von Thun and Gillette [100] and Xu and Zhang [101] methods, which account for dam erodibility as a key parameter, two sub-scenarios are examined, assuming medium and high erodibility. Finally, the last three scenarios apply the methods embedded in BASEbreach software (Macchione, Peter, Peter Calibrated).

**Table 1**
Total rainfall, flood peaks and flood volumes for various time scales.

| Rainfall duration | 10,000-years rainfall (mm) | Flood volume over the upstream basin (m$^3$) | Flood volume over the reservoir area (m$^3$) | Total volume (m$^3$) |
|---|---|---|---|---|
| 10 min | 46.6 | 2114 | 30,580 | 32,694 |
| 24 h | 455.0 | 86,551 | 245,685 | 332,237 |
| 72 h | 648.9 | 133,594 | 350,409 | 484,003 |

**Table 2**
Examined piping scenarios.

| Methodology | Scenario |
|---|---|
| Software: HEC-RAS | |
| MacDonald et al. (1984) | 1 |
| Froehlich [97] | 2 |
| Froehlich [98] | 3 |
| *Dam erodibility: Medium* | |
| Von Thun and Gillette [100] | 4a |
| Xu and Zhang [101] | 5a |
| *Dam erodibility: High* | |
| Von Thun and Gillette [100] | 4b |
| Xu and Zhang [101] | 5b |
| Software: BASEbreach | |
| Macchione [104] | 6 |
| Peter [105] | 7 |
| Peter Calibrated | 8 |

Input data include geometric properties and characteristic elevations (Table 3), and the elevation-storage function of the reservoir. Furthermore, for scenarios 1–7, three erosion-related breach parameters (final bottom width, left-right side slope, and formation time of the breach), are required, which are computed via the regression equations of HEC-RAS (Table 4). On the other hand, scenarios 8–10, utilizing BASEbreach, use a reservoir shape parameter, which is set to 1 [122,123].

#### 4.2.2. *Resulting flood hydrographs by dam breach scenarios*

From the piping analyses conducted using HEC-RAS and BASEbreach, the outflow hydrographs for each scenario are produced, which are depicted in Fig. 7. The flood peaks across the ten scenarios range from 4638 to 10,188 $m^3/s$, while the flood volumes are identical, since the entire stored water is released, after the dam breach (equal to the reservoir capacity up to the MOL, i.e. 10.25 $hm^3$).

It is observed that the Froehlich [97], [98] and Von Thun & Gillette methods (medium erodibility) yield similar results regarding the peak magnitude and time to peak of the hydrograph. In contrast, the Xu & Zhang (medium erodibility) and MacDonald & Langridge-Monopolis methods produce smaller peaks at later times. The three methods included in BASEbreach (Macchione, Peter, and PeterCal) result to similar peak magnitudes, but at earlier times. For the two methods (Von Thun & Gillette, Xu & Zhang) where high erodibility scenarios were also examined, the resulting hydrographs exhibit higher peaks appearing earlier compared to the medium erodibility scenarios, as expected.

Fig. 7 also depicts the average scenario (indicated with a dashed line), calculated as the mean of all 10 examined scenarios. It is noted that its peak (4427 $m^3/s$) is even smaller than the one of the most favorable scenario 5a, which is explained by smoothing effects across different hydrograph shapes and associated timing properties.

#### 4.2.3. *Validation through empirical relationships for flood peaks*

Based on the recommendations outlined in the HEC-RAS manual [90], the above results should be validated by comparing the flood peaks with empirical regression equations for flood peaks. Tables 5 and 6 present the empirical relationships used for comparative purposes and the associated parameter values, respectively.

The results for all examined equations are also presented in Table 6. It is observed that these are generally close to the flood peaks derived from the simulation models and those from the empirical relationships. The analytical simulation models yield an average peak discharge of 6744 $m^3/s$ and a maximum of 10,188 $m^3/s$, while the empirical relationships produce an average of 7908 $m^3/s$ and a maximum of 15,865 $m^3/s$.

This comparative exercise serves as a form of validation in the absence of historical data, given that the upper reservoir is a planned

**Table 3**
Input data for piping scenarios.

| Parameter | Value |
|---|---|
| Dam crest elevation (m) | 561 |
| Breach bottom elevation (m) | 523 |
| Pool elevation at failure (m) | 560 |
| Pool volume at failure ($hm^3$) | 10.25 |
| Breach weir coefficient | 1.44 |
| Piping coefficient | 0.50 |
| Dam crest width (m) | 5 |
| Slope of US dam face Z1 H:V | 1 |
| Slope of DS dam face Z1 H:V | 1 |
| Dam material | Uniform |
| Dam type | Uniform/stratified homogeneous |
| Dam erodibility | Medium/High |
| Set time (hrs) | 0:00 |

**Table 4**
Erosion parameters of the breach calculated from regression equations.

| Scenario Nr. | Methodology | Final breach width (m) | Side slopes of breach (H:V) | Breach formation time (h) |
|---|---|---|---|---|
| 1 | MacDonald et al. (1984) | 50 | 0.5 | 1.2 |
| 2 | Froehlich [97] | 29 | 0.9 | 0.5 |
| 3 | Froehlich [98] | 28 | 0.7 | 0.47 |
| Dam erodibility | | **Medium** | | |
| 4a | Von Thun and Gillette [100] | 116 | 0.5 | 0.99 |
| 5a | Xu and Zhang [101] | 28 | 0.6 | 1.32 |
| Dam erodibility | | **High** | | |
| 4b | Von Thun and Gillette [100] | 116 | 0.5 | 0.56 |
| 5b | Xu and Zhang [101] | 38 | 1.05 | 0.69 |

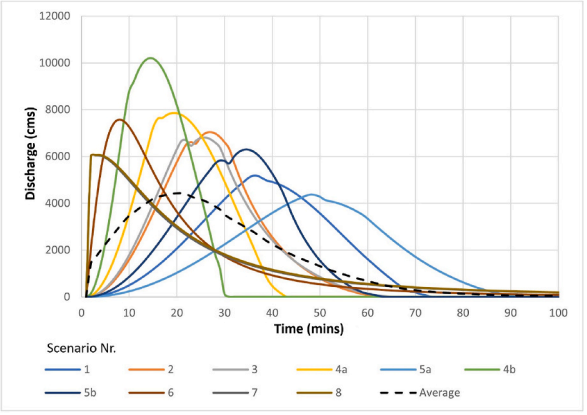


**Fig. 7.** Dam breach hydrographs for each piping scenario.

**Table 5**
Empirical relationships used for validating the results of analytical simulations.

| Method | Empirical formula | Qmax ($m^3/s$) |
|---|---|---|
| USBR (1982) | $Q = 19.1(h_w)^{1.85}$ | 15,213 |
| MacDonald and Langridge-Monopolis [99] | $Q = 1.154(V_w h_w)^{0.412}$ | 3951 |
| Froehlich [124] | $Q = 0.607{V_w}^{0.295}{h_w}^{1.24}$ | 6251 |
| Xu and Zhang [101] | $\frac{Q}{\sqrt{g{V_w}^{5/3}}} = 0.175\left(\frac{h_d}{h_r}\right)^{0.199}\left(\frac{{V_w}^{1/3}}{h_w}\right)^{-1.274} e^{B_4}$ | 6171(medium)<br>8916 (high) |
| SCS [125] | $Q = 16.6(h_w)^{1.85}$ | 13,222 |
| Hagen [126] | $Q = 0.54(Sh_d)^{0.5}$ | 10,516 |
| Singh and Snorrason [127] (1) | $Q = 13.4(h_d)^{1.89}$ | 12,969 |
| Singh and Snorrason [127] (2) | $Q = 1.776(S)^{0.47}$ | 3503 |
| Costa [91] (1) | $Q = 1.122(S)^{0.57}$ | 12,111 |
| Costa [91] (2) | $Q = 0.981(Sh_d)^{0.42}$ | 3978 |
| Costa [91] (envelope) | $Q = 2.634(Sh_d)^{0.44}$ | 15,865 |
| Evans [128] | $Q = 0.72{V_w}^{0.53}$ | 3741 |

infrastructure. The close alignment of simulated peaks with empirical expectations lends credibility to the modeled hydrographs.

#### 4.2.4. *Development of a representative hydrograph*

The exceptional variability of the ten outflow hydrographs shown in Fig. 7 highlights the significant uncertainty associated with failure mechanisms, their modeling, and prevailing conditions. Based on these scenarios, a representative hydrograph is also developed, to reflect a "medium probability" breach event.

The representative hydrograph considers the average one as a reference for extracting the temporal profile of the flows. Under this premise, the peak of the representative hydrograph is set to coincide with the peak of the average hydrograph, which occurs 21 min after the breach initiation. Similarly, the timing of the *k*-th highest values of both the average and representative hydrographs is aligned. Once the timing of the representative hydrograph is established based on the average hydrograph, the ten scenarios are sorted

**Table 6**
Input parameters for estimating peak discharge due to dam breach.

| Parameter | Description | Value |
|---|---|---|
| $h_w$ (m) | Height of water volume above the breach initiation point | 37 |
| $V_w$ ($m^3$) | Water volume above the breach initiation point | $10.25 \times 10^6$ |
| $S$ ($m^3$) | Reservoir storage above the breach initiation point | $10.25 \times 10^6$ |
| $h_d$ (m) | Dam height | 38 |
| *Parameters for the*Xu and Zhang [101] *method* | | |
| $h_r$ | Characteristic height separating large and small dams | 15 |
| $b_3$ | Coefficient for earthen dams | −0.649 |
| $b_4$ | Coefficient for piping scenarios | −1.039 |
| $b_5$ high | Coefficient for high erodibility | −0.007 |
| $b_5$ medium | Coefficient for medium erodibility | −0.375 |
| $B_4$ high | b3 + b4 + b5 high | −1.695 |
| $B_4$ medium | b3 + b4 + b5 medium | −2.063 |

in descending order, and their average is calculated. The first value, corresponding to the average peak discharge of the ten scenarios (6744 $m^3$/s), is assigned to time step 21. The remaining average values are positioned accordingly, following the already determined temporal profile.

Fig. 8 compares the representative hydrograph with the average one, as well as with the ten individual outflow scenarios. Interestingly, the representative hydrograph is quite close to the hydrograph corresponding to the method by Froehlich [98], generally considered as the most recommended in the literature.

## 5. Flood wave propagation between the upper and the lower reservoir

While previous studies have offered valuable insights into dam-break scenarios and cascade reservoir systems, many have focused primarily on single-reservoir configurations or cascades lacking the bidirectional flow complexity of pumped-storage hydropower (PSH) (e.g., Ref. [10,33]). Our study expands upon this foundation by exploring the implications of upper dam breaches within PSH systems, where operational dynamics, limited spatial buffering, and rapid wave propagation demand tailored modeling strategies.

### 5.1. Model inputs and assumptions

The modeling of flood wave routing resulting from dam breach scenarios was conducted using HEC-RAS 6.4.1. Three characteristic outflow hydrographs were analyzed, namely the most favorable out of ten breach simulation scenarios (Xu & Zhang method, with medium dam erodibility), the most adverse one (Von Thun & Gillette method, with high dam erodibility), and the so-called as representative (section 4.2.4).

The three hydrographs were set as upstream boundary conditions to the HEC-RAS hydrodynamic model, to simulate their routing across the downstream region of the dam up to the Sfikia reservoir (2D flow area), thus providing critical insights into the flood dynamics. Key inputs and assumptions were: (a) a computational grid of 50 × 50 m sized finite volume cells, comprising 1070 elements, relying on a DTM by the Hellenic Cadastre, with spatial resolution 2 × 2 m; (b) a time step of 1.0 s, considering the CFL criterion, (c) a Manning roughness coefficient of 0.06 for floodplain areas, as advised by Chow (1959), and (d) a stage-time curve at the downstream boundary, by setting the stage to the Maximum Operating Level (MOL) of Sfikia reservoir (+146.0 m).

### 5.2. Routed hydrographs

Due to the steep terrain slopes and the relatively small distance, the shape of the routed hydrographs is quite similar to the upstream

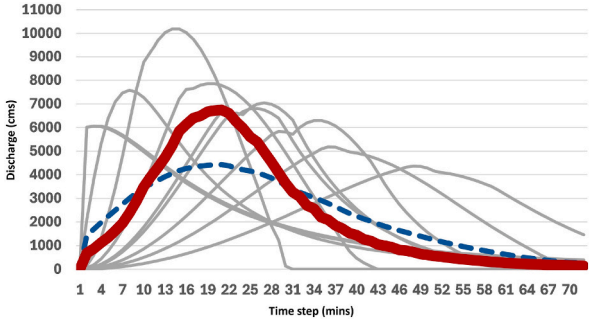


**Fig. 8.** Representative hydrograph (thick line, red color), contrasted to the ten outflow scenarios (thin lines, gray color) and their average (blue dashed line).

ones. In this respect, the lag time is minimal (approximately 5 min), and the peak flows are only slightly attenuated. Specifically, in the adverse, favorable and representative scenarios, the peak discharge decreases by only 0.2 %, 0.4 % and 0.2 %, respectively (Fig. 9).

These hydrographs are utilized next, to assess the cascade impacts on the Sfikia reservoir and associated hydraulic structures. The corresponding flood volumes range from 6.9 to 8.3 $hm^3$, which are smaller than the initial water volume released due to the Brava dam breach (10.5 $hm^3$). This discrepancy arises because part of the water is retained along the flow path due to the storage capacity of the stream.

### 5.3. Practical implications based on velocity and arrival time maps

Fig. 10 depicts the simulated maximum velocities and arrival times between the upper reservoir (Brava) and the lower one (Sfikia), for the representative dam breach scenario.

Key remarks drawn from the velocity map are:

- *Velocity distribution*: Across the model domain from the Brava main dam to the Sfikia reservoir, the maximum velocities (>21 m/s) are concentrated near the dam's breach point, diminishing progressively downstream.
- *Spatial patterns*: The velocity gradients along the flow path illustrate the influence of topographical and channel constrictions. These reflect rapid deceleration as the flood wave transitions from steep slopes to flatter terrain near the reservoir.
- *Impact on Sfikia reservoir*: Upon entering the reservoir, velocities drop significantly, indicating a dispersion of the flood's kinetic energy. This transition suggests a potential reduction in erosional forces within the reservoir's vicinity.
- *Implications for structures*: The high velocities near the dam and along narrow channels pose critical risks to hydraulic infrastructure and riverbank stability. These zones demand robust protective measures.

Regarding the arrival time map, key conclusions are:

- *Flood wave propagation*: The flood wave reaches the Sfikia reservoir within a short time frame (5–10 min for most areas), as result of the steep terrain and the large velocities.
- *Critical timing*: The rapid wave propagation leaves minimal time for emergency response measures, emphasizing the need for preemptive risk management strategies.
- *Temporal distribution*: Areas closer to the dam breach experience flooding within 3 min, while zones near the reservoir experience delays up to 20 min. This progression underscores the time-sensitive nature of inundation impacts.
- *Emergency planning*: The rapid arrival times highlight the necessity for real-time monitoring systems and advanced warning protocols, to protect vulnerable downstream areas.

## 6. Assessment of cascade impacts on the lower reservoir

### 6.1. Problem setting

Following the generic framework rational for assessing cascading effects across PSH systems, two adverse phenomena over the lower reservoir and associated structures are examined, namely: (a) the temporal storage of the arriving flood hydrographs and their routing downstream via the turbines and spillways, (b) a tsunami-like wave propagating through the reservoir and reaching the Sfikia dam. The associated processes are analyzed separately, to assess the risk of overtopping the Sfikia dam (crest elevation +150.7 m).

Specifically, the tsunami phenomenon is approximated via two approaches (theoretical and semi-empirical), as proposed in the generic framework, since the overall problem is subject to major complexities and limited global experience. Both approaches aim at representing the wave route between characteristic points A (entry of hydrograph), B, C, D and E (dam site), as shown in Fig. 11.

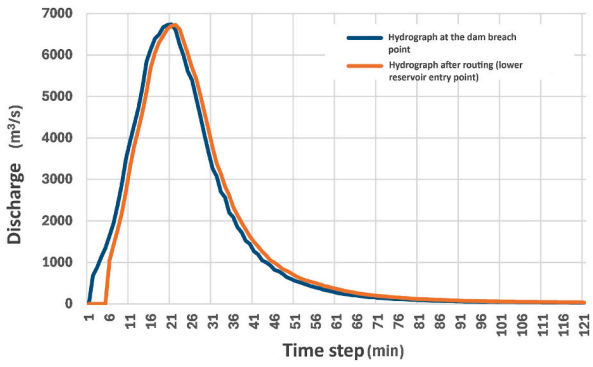


**Fig. 9.** Comparison of upstream (at the breach point) and downstream routed hydrograph at the lower reservoir entry point for the representative scenario.

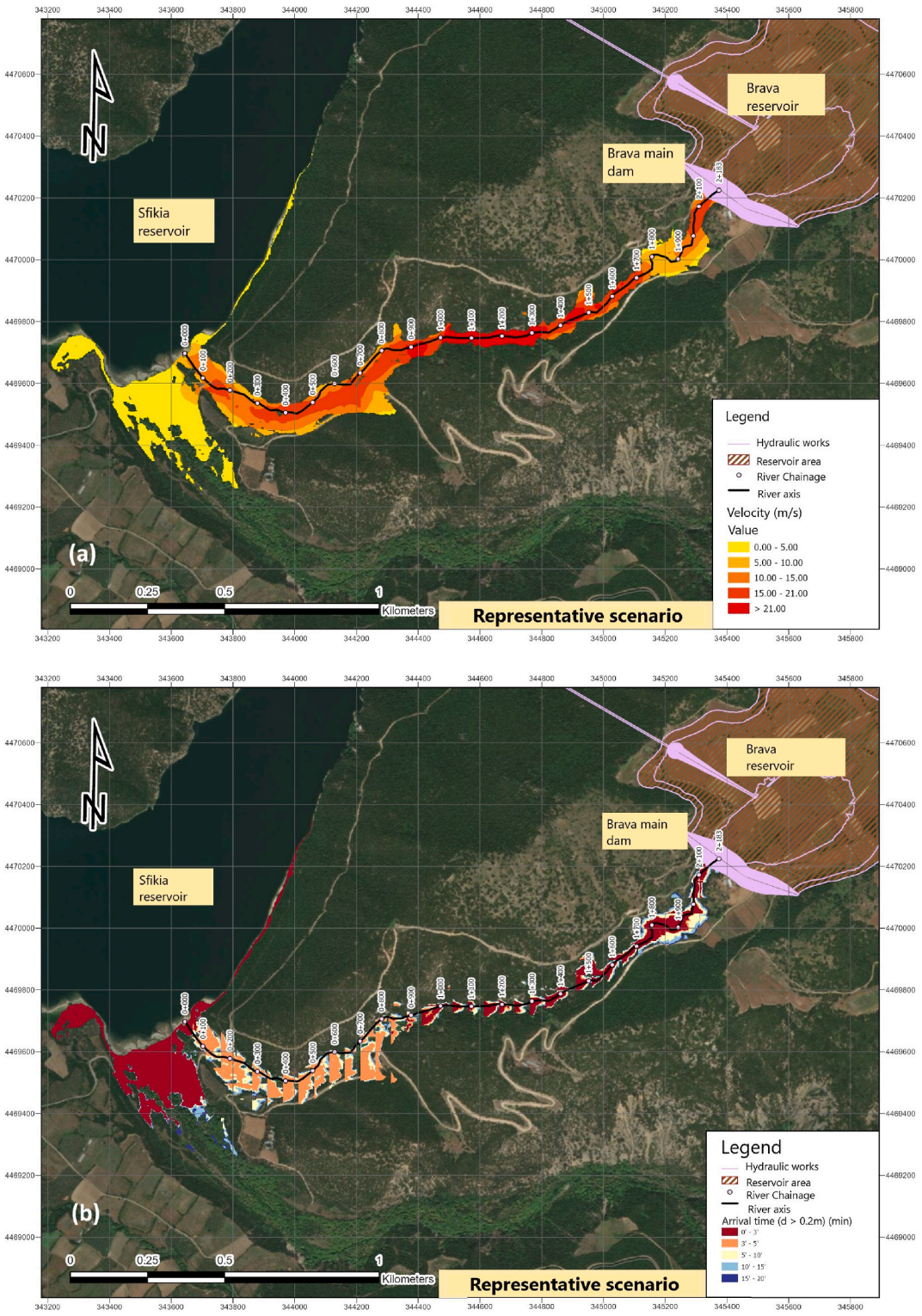


**Fig. 10.** (a) Maximum velocity, and (b) arrival time for the area between Brava and Sfikia reservoirs corresponding to the representative dam breach scenario of Brava (Basemap source: ESRI et al., 2025).

### 6.2. Flood hydrograph routing through Sfikia reservoir

Four scenarios were formulated, as combinations of two input hydrographs caused by the upper dam breach, i.e., representative and most adverse, and two operational modes of the entire Aliakmon Hydropower Complex, i.e., idle and under design flood conditions.

The *idle mode* assumes that both the hydropower stations and the spillways are closed, thus there are no water exchanges among the individual reservoirs. Under this premise, Sfikia does not receive inflows from the upstream reservoir (Polyphyto), neither releases water to the downstream one (Asomata). This means that to enforce the outflow control structures operating in their full capacity (600 $m^3/s$ for the tow turbines and up to 1600 $m^3/s$ for the gated spillway) and convey with safety the wave arriving suddenly due to upper dam damage, a reasonable time lag must be accounted for. In this respect, it is assumed that the turbines need 10 min to become fully active, with the spillway gates opening gradually over 30 min. This period represents the most adverse case, due to increased friction on the rubber seals.

In contrast, the *flood design mode* assumes that all control structures across the Aliakmon Complex are fully operative at their maximum capacity. Therefore, apart from the inflow hydrograph due to the dam breach, Sfikia also receives a constant inflow of 1720 $m^3/s$, corresponding to the combined design discharge of the turbines and the spillway of Polyphyto. At the same time, the power station of Sfikia is fully active, thus releasing 600 $m^3/s$ to the downstream reservoir, and the spillway gates are also fully open.

The rest inputs to run the routing problem are the initial reservoir level at the beginning of the routing process, which is set to the

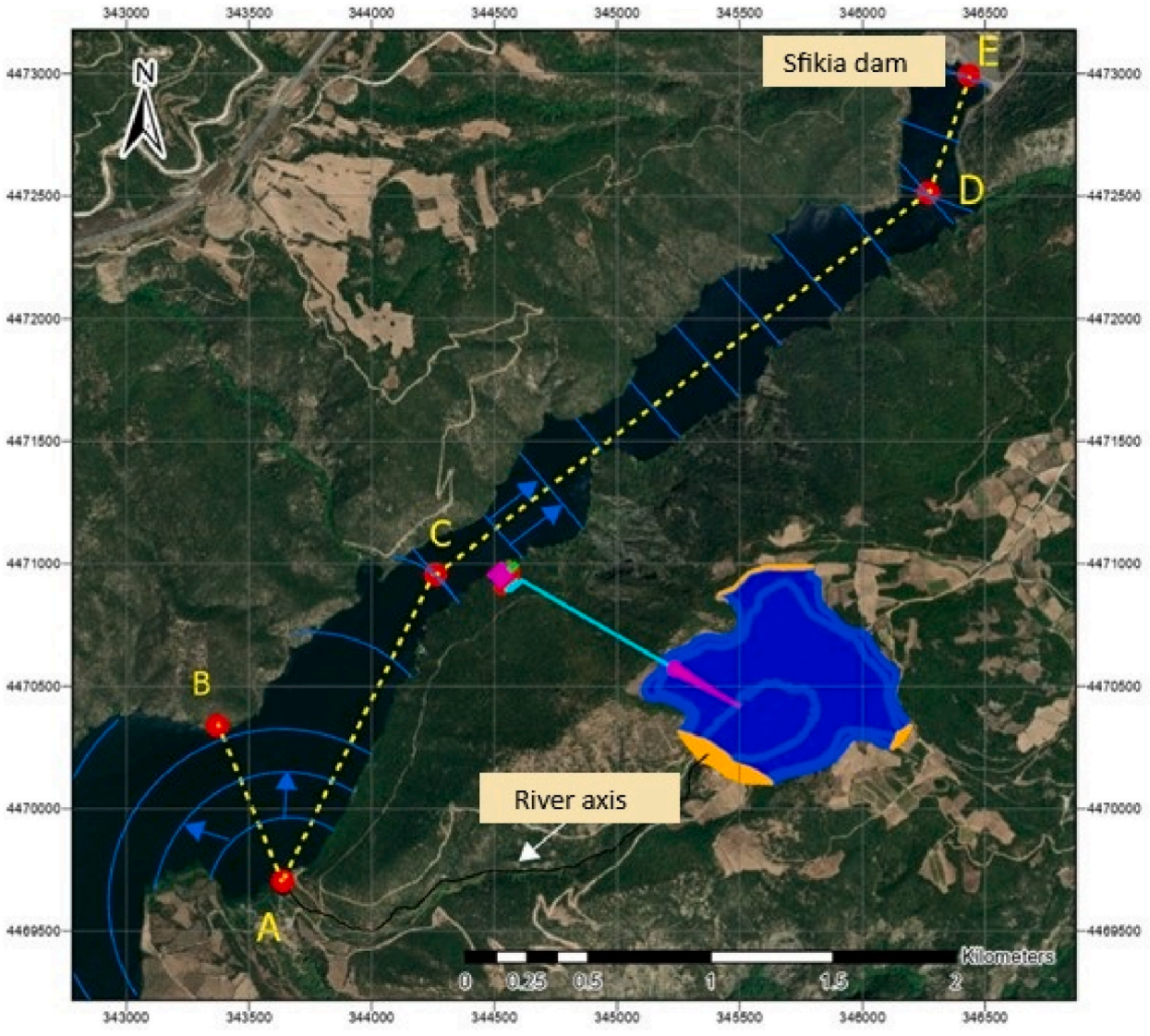


**Fig. 11.** Geometry of Sfikia reservoir and characteristics points illustrating the route of the wave produced by the water volume arriving at point A (Basemap source: ESRI et al., 2025).

MOL (+146.0 m), the elevation-storage function of the reservoir and the discharge formula of the gated spillway.

To derive the stage-storage relationship, a power-type expression (eq. (3)) is fitted to the higher storage and elevation values, by setting $z_b = 85.0$ m. The optimized scale and shape parameter values were $\kappa = 0.00152$ and $\lambda = 2.698$, respectively. The quite large $\lambda$ aligns with the canyon-like topography of the reservoir [110].

The operational characteristics of the spillway system were derived from an experimental study, conducted in the context of its design [129]. Based on this, the following stage-discharge nomograph was applied, corresponding to free flow conditions (fully open spillway gates):

$$q = 47.281\ (z - 137.0)^{1.545} \tag{10}$$

It is observed that the exponent is slightly higher than the theoretical value of 3/2. As explained in section 2.3, this discrepancy arises because the theoretical equation (3) incorporates the kinetic energy term. Under partially opened gates, eq. (6) is applied which accounts for the time-varying height of gate opening, $B$, by setting $c = 0.70$, $W = 14.4$ m (gate's width), $T = 9.0$ m (trunnion height, equal to the gate's height), $TE = 0$ (default value), $BE = 0.90$ and $HE = 0.65$. The two exponent parameters, i.e. $BE$ and $HE$ were assigned after a trial-and-error approach, such as the discharges for fully opened gates (i.e., $B = T$) are identical to the values estimated by eq. (8), for free flow conditions.

The key results of the four scenarios are summarized in Table 7, while for two of them, the inflow, outflow and water level time series are also depicted (Fig. 12). In the most realistic scenario, where the most representative breach hydrograph is routed and the system is in idle mode, the maximum water level reaches 147.3 m, thus slightly above the maximum design flood level (+147.0 m) and clearly lower than the dam crest (+150.7 m). Even under the most unfavorable conditions (worst-case breach hydrograph, under design flood operation mode), the reservoir level lifts to a maximum elevation of 148.1 m, within approximately half an hour. Consequently, there is still a quite large margin of ~2.6 m before reaching the dam crest, which may be viewed as a safe buffer.

### 6.3. Assessment of cascade impacts due to tsunami

#### 6.3.1. Theoretical approach

The simulation of the impulse wave generated by the sudden water influx due to the Brava dam failure was conducted along the axis depicted in Fig. 14. The analysis was carried out at a midpoint location ($x = 330$ m) over a simulation period of 200 s. Key inputs, derived from the hydrodynamic analysis for the adverse scenario, were the collapsing block volume, $V_{box} = 8.32$ hm$^3$, its density, $\rho_{box} = 1000$ kg/m$^3$, the downstream length, $L = 2183$ m, the outflow depth d = 7 m, and the initial velocity, with a resultant value Vtot = 7 m/s, analyzed to Vhor = 6.93 m/s and Vvert = 0.97 m/s, for a slope equal to 14 %. The geometrical properties of the simplified collapsing volume, namely its width and its equivalent length, were estimated by $w = V_{box}/(L\,d)$ and $Leq = V_{box}^{1/3}$.

The solution to the differential equation (eq. (7)) yielded a maximum wave height of approximately 12.4 m at the midpoint, as shown in Fig. 13. Subsequent analyses accounted for attenuation mechanisms, specifically bottom friction and diffraction, along the 4400 m distance to the Sfikia dam (Fig. 14). Three scenarios were analyzed for three bottom friction coefficients, i.e. 0.05, 0.50 and 1.00. A total diffraction loss coefficient of 42 % was estimated based on the interaction of the wave with riverbanks treated as impermeable barriers, according to the coefficients given by Goda [118].

The key results of the theoretical analysis, in terms of initial wave heights at the dam site and associated heights after diffraction, estimated maximum run-up and associated water level, as well as safety margins (i.e., distance from dam crest), are summarized in Table 8. While the wave heights at the dam are expected to cause significant run-up (eq. (9)) along the dam's inclined surface of sloe $\beta = 26.6°$ (Fig. 11, cross section DE), this remains within acceptable limits.

#### 6.3.2. Semi-empirical approach

The semi-empirical approach follows the methodology of Evers et al. [25], which is briefly explained in section 2.5.3. Wave run-up is analyzed at positions B and E of Fig. 11, considering wave characteristics and site-specific topographic features, such as slope angle $\beta$

**Table 7**
Assumptions and key outcomes of the four scenarios examined within the routing modelling through the lower reservoir (Sfikia).

| Scenario | 1 | 2 | 3 | 4 |
|---|---|---|---|---|
| Operation mode | *Idle* | | *Design flood* | |
| Input hydrograph due to dam breach | *Representative* | *Adverse* | *Representative* | *Adverse* |
| Peak inflow (m$^3$/s) | 6729 | 10,169 | 6729 | 10,169 |
| Inflow from Polyphyto (m$^3$/s) | 0 | 0 | 1720 | 1720 |
| Time lag for turbine opening (min) | 10 | 10 | 0 | 0 |
| Time lag for gate opening (min) | 30 | 30 | 0 | 0 |
| Total maximum inflow (m$^3$/s) | 6729 | 10,169 | 8449 | 11,889 |
| Maximum outflow (m$^3$/s) | 2129 | 2171 | 2179 | 2206 |
| Maximum spillway discharge (m$^3$/s) | 1529 | 1571 | 1579 | 1606 |
| Attenuation ratio | 31.6 % | 21.4 % | 25.8 % | 18.6 % |
| Maximum reservoir level (m) | 147.25 | 147.81 | 147.77 | 148.06 |
| Distance from dam crest (m) | 3.45 | 2.89 | 2.93 | 2.64 |
| Peak level rise time (min) | 31 | 23 | 47 | 27 |

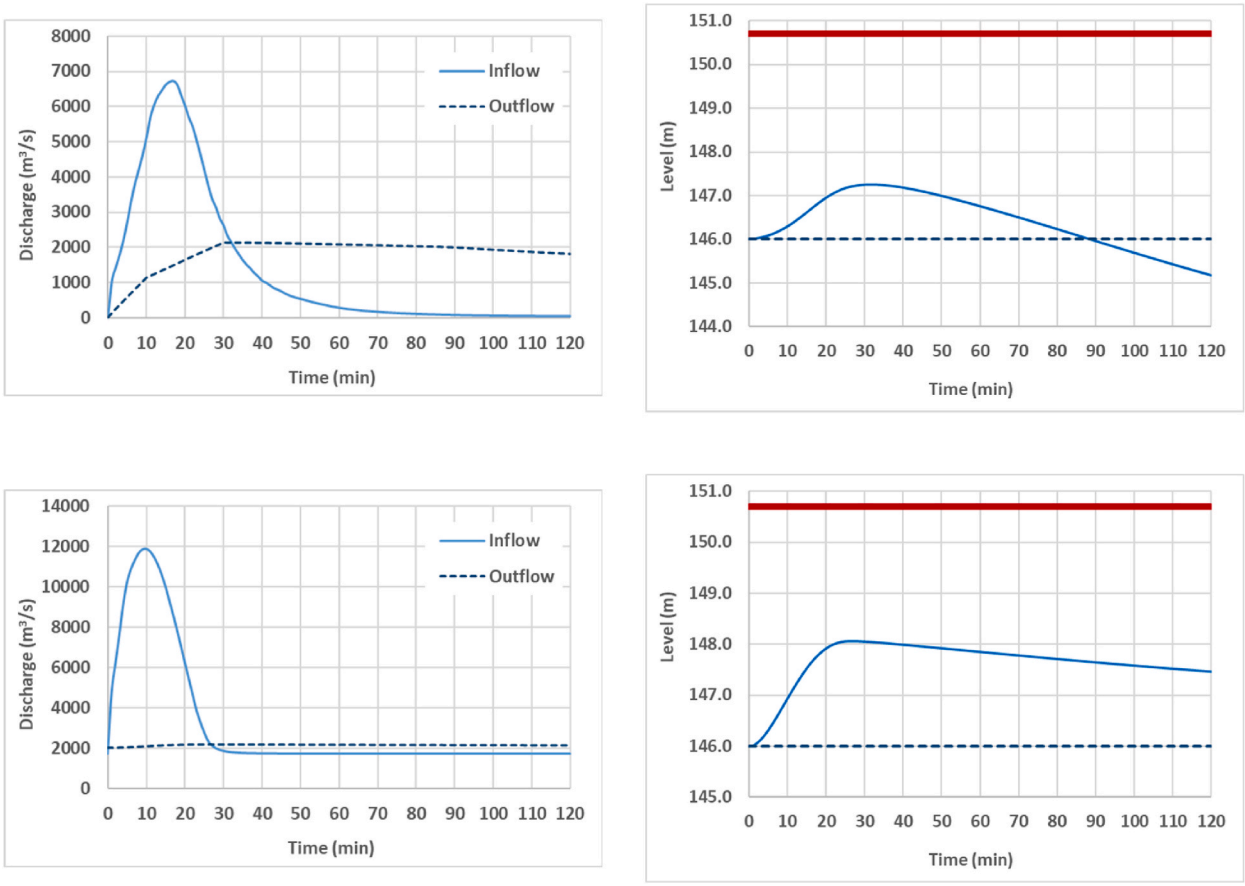


**Fig. 12.** Time series of inflows vs. routed outflows (left) and reservoir level (right) for scenarios 1 (upper panel) and 4 (lower panel). The red line indicates the dam crest.

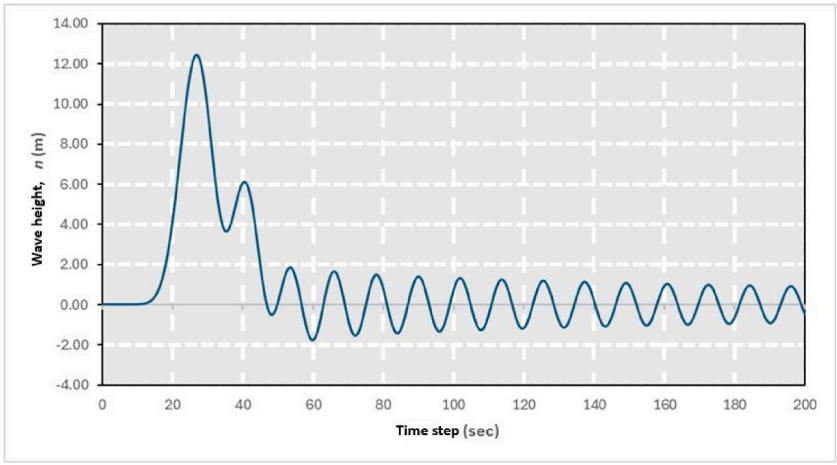


**Fig. 13.** Results of wave height differential equation solution.

and water depth $h$. The detailed geometrical characteristics across all cross-sections are depicted in Fig. 15.

The wave generation and propagation are influenced by several key factors. The slide impact velocity is estimated at $V_s = 7.0$ m/s, derived from the adverse HEC-RAS scenario. The landslide volume ($\bar{V}_s$) is calculated as $\bar{V}_s = 8.32$ hm$^3$, with an average thickness $s =$ 7.0 and width $w = 544.5$ m. At the point of impact A, the water depth is 30 m, increasing to 50 m at location B. Using these parameters

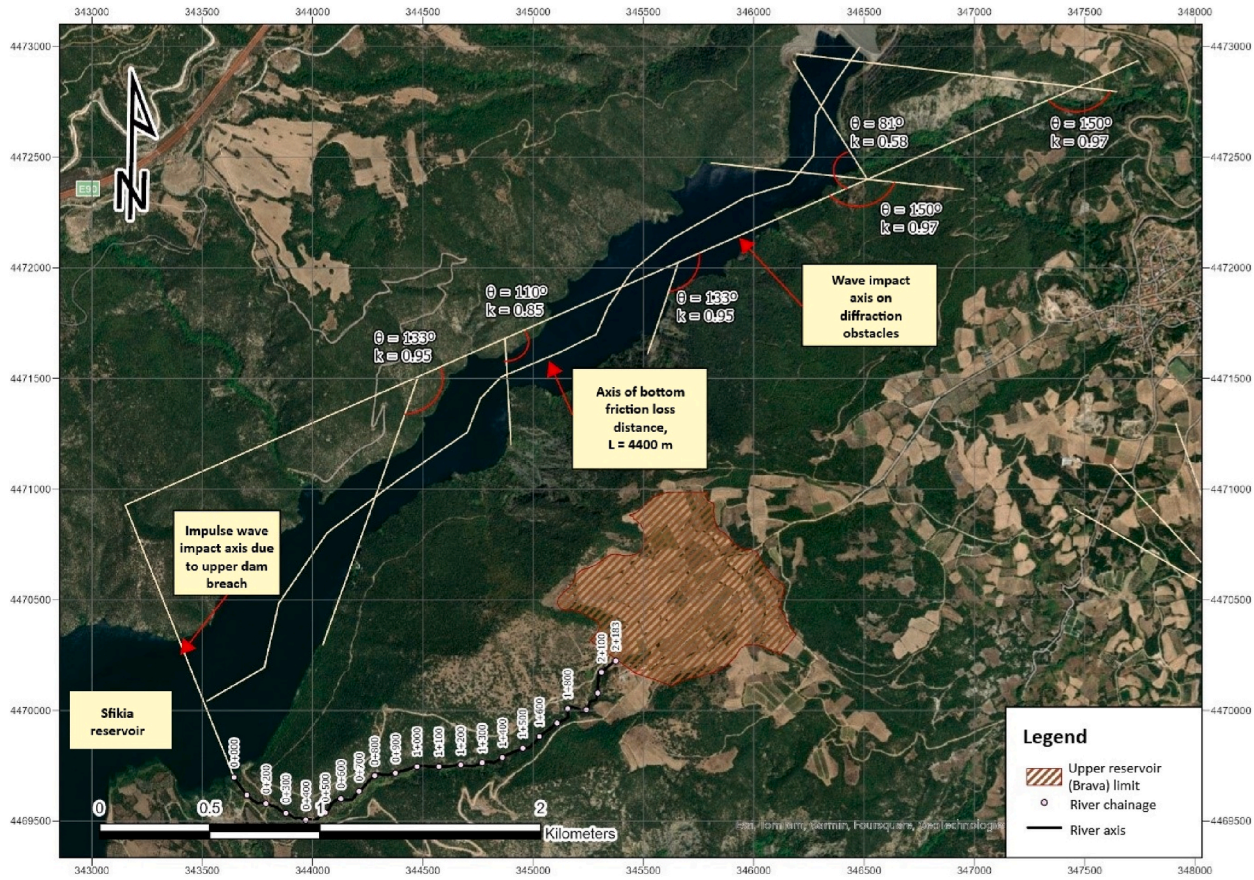


**Fig. 14.** Diffraction angles and coefficients, and bottom friction loss distance (Basemap source: ESRI et al., 2025).

**Table 8**
Key results of theoretical analysis for three bottom friction coefficient values.

| Bottom friction coefficient, $f_w$ | Initial wave height at the dam (m) | Wave height after diffraction (m) | Run-up, $R$ (m) | Maximum water level (m) | Distance from dam crest (m) |
|---|---|---|---|---|---|
| 0.05 | 3.5 | 1.5 | 3.7 | 149.7 | 1.0 |
| 0.50 | 1.9 | 0.8 | 2.0 | 148.0 | 2.7 |
| 1.00 | 1.3 | 0.5 | 1.4 | 147.4 | 3.3 |

along with radial distance and wave propagation angle for the points of interest, wave propagation characteristics are analyzed with 3D equations for locations B and C, while 2D attenuation factors are applied for downstream locations C, D, and E.

The results of the wave propagation analysis show significant attenuation along its path. At location B, lying 660 m from the impact point, with $0^o$ wave propagation angle, the first wave crest amplitude is calculated to be 6.4 m. As the wave reaches location C (1392 m distance, wave propagation angle $48^o$), the wave crest amplitude decreases to 1.9 m, as influenced by radial dispersion and bottom friction. By the time the wave reaches the dam, at location E (4440 m from impact point A), the amplitude is further reduced to 0.55 m. This progressive attenuation underscores the critical role of friction and geometric dispersion in dissipating wave energy over distance.

Wave run-up ($R$) is estimated at critical locations B and E through eq. (9). At location B, the run-up height is calculated to be approximately 18 m, while at location E, it reduces to only 1.41 m, thus close to the favorable scenario of the theoretical approach.

The wave arrival times at key locations are also very critical. In this respect, it is estimated that the wave requires 31 s to travel from location A to B, while it reaches the dam location E after only 208 s, thus much earlier than the time-to-peak of the routed hydrograph (at least 27 min, for the most extreme scenario; Fig. 12). This outcome is of major importance, since a hypothetical coincidence of the two peaks, i.e. from the flood routing and the tsunami wave, may lead to overtopping of Sfikia dam, with potentially catastrophic cascade effects to the dam and the downstream hydrosystem.

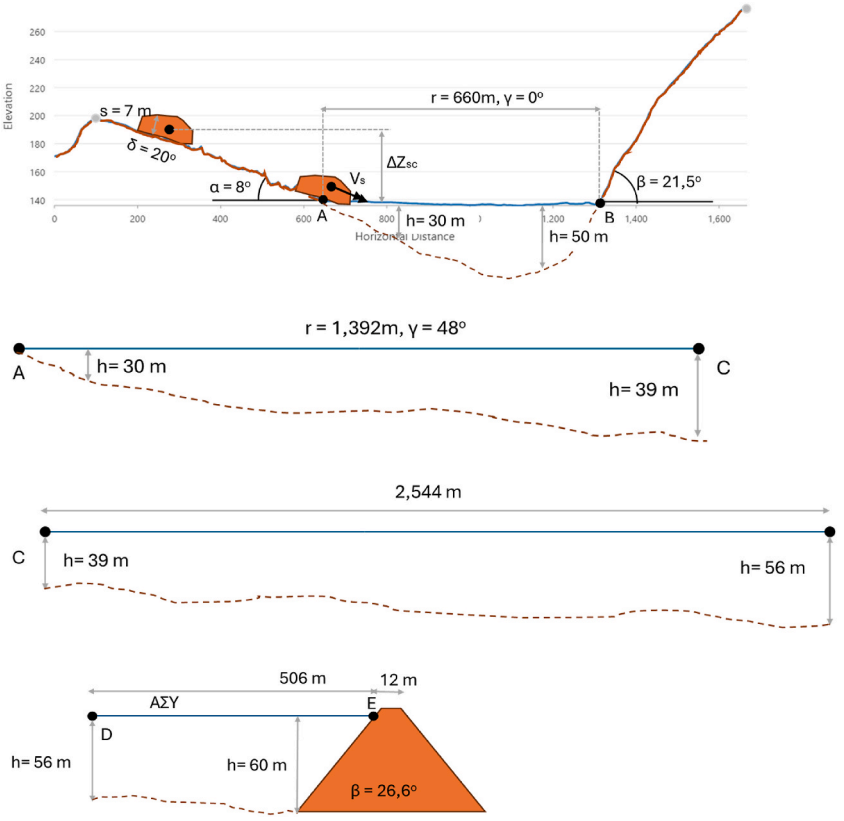


**Fig. 15.** Layout of cross-sections AB, AC, CD, and DE (from top to bottom).

### *6.4. Discussion on tsunami modelling deficiencies*

#### *6.4.1. Theoretical approach*

While the bottom friction is considered the primary mechanism for wave attenuation, several other mechanisms also contribute to energy dissipation. Turbulent diffusion [130] plays a key role as the wave propagates, particularly at the wave front and within the water column, where turbulent motion transforms wave energy into heat, gradually reducing wave height. Surface tension and viscosity [131,132] at the water-air interface also lead to energy dissipation, with these effects being more pronounced for smaller waves or those with shorter wavelengths. Wave breaking [133,134,135] is another significant mechanism; steep and high waves may break during propagation, dispersing a substantial portion of their energy as turbulence.

Geometric dispersion is observed as waves radiate radially from the source, distributing their energy over a larger area and reducing wave height [136,137]. This effect is highly dependent on the shape of the reservoir and its boundaries. Similarly, absorption by vegetation or rugged shores [60,138,139] can attenuate wave energy, particularly in reservoirs surrounded by natural features. Compared to artificial or smooth surfaces, natural shores tend to absorb more energy, contributing to wave attenuation. Interaction with solid boundaries, such as irregular coasts or cliffs, often results in partial reflection or scattering of the wave, redistributing energy and diminishing wave intensity.

Relief variations across the reservoir bed definitely influence wave speed and amplitude through refraction, thus redistributing wave energy and reducing intensity [140,141]. Finally, the interaction of waves with suspended sediments by landslides or debris flows adds another layer of energy dissipation, due to mixing and particle-fluid interactions [142,143].

#### *6.4.2. Semi-empirical approach*

This approach, although more comprehensive, is also subject to inherent uncertainties and limitations. For instance, the differences between idealized geometries of reservoirs and channels (prismatic, channel form geometry, rectangular basin shape) and the omission of key processes, such as volumetric displacement, reflection, and shoaling or constriction of the wave propagation at the dam abutments may introduce inaccuracies. Simplified assumptions regarding radial propagation and energy dissipation may also affect the accuracy of wave attenuation estimates. Additional uncertainties originate from the omittance of other important factors, such as sediment interactions, shoreline conditions, and depth variations.

Despite these limitations, this approach provides a valuable framework for representing wave generation, propagation, attenuation, and wave run-up processes. Nevertheless, the identified uncertainties highlight the need for further validation through detailed

numerical simulations/CFD analyses [144,145], which could refine the model results and eventually enhance the reliability of hazard assessments, both for the case of upper dam failures and also for landslide phenomena in reservoirs.

## 7. Conclusions

This research manifests a generalized framework for assessing the cascading impacts of the upper dam failure across PSH schemes, under the broader prism of *resilience assessment of critical infrastructures*. The overall challenge is to describe and interpret the full chain of cascade effects, by combining models of different levels of maturity, complexity, data specifications, user decisions and computational burden. The existence of multidimensional uncertainties across all modelling steps requires a balanced view, to ensure a faithful representation of the individual processes and their interplays, eventually resulting in useful implications for practicians.

The framework was stress-tested to a planned system in Greece, where the failure of the upper dam may cause dramatic effects to one of the most vital water-energy systems of the country, i.e. Aliakmon Hydropower Complex. Key findings include:

1. Dam breach modeling via empirical and semi-empirical tools reveals wide discharge variability, justifying the scenario-based approach under uncertainty.
2. Flood wave propagation from the upper to lower reservoir occurs rapidly (order of magnitude of a few minutes), leaving minimal response time.
3. Routing analyses confirm that even under worst-case inflows, the lower dam (Sfikia) maintains a safety margin.
4. Impulse wave simulations, using both theoretical and semi-empirical methods, show that tsunami run-up does not threaten overtopping.
5. No synchronization was observed between peak routed flows and impulse wave arrival times, which reduces compound risk.

Policy Implications:

- Early warning systems must account for short arrival times.
- Regular maintenance of turbine and spillway operation is critical for emergency response.
- Real-time monitoring of upper reservoir integrity can significantly improve preparedness.

These findings inform infrastructure design, emergency protocols, and energy policy aiming at resilience and sustainability.

We highlight that the abovementioned risk assessment procedure was hold under the premise that there will be sufficient time for all essential actions, i.e., for accessing the spillway, notifying the Safety Officer, and allowing a slow and controlled opening to ensure a smooth flow transition. This implies the need for systematic monitoring of all critical elements of the PSH scheme, enabling the immediate notification of the operators and authorities of Aliakmon Complex, in the case of a breach of the Brava dam.

Nevertheless, it is important to acknowledge the significant uncertainties associated with the cascade phenomena, as well as the inherent simplifications and assumptions of the underlying modeling procedures. In fact, the major uncertainties in wave attenuation mechanisms and flood routing highlight the need for further refinement of impulse wave simulation approaches, even if the proposed modeling arsenal is providing strong "weapons" for the day-to-day engineering practice. Our findings emphasize the importance of detailed hydrodynamic assessments to support the safe operation and structural resilience of pumped-storage hydropower systems. In this way, future research should take advantage of advanced numerical modeling to improve risk assessments and optimize mitigation strategies.

## CRediT authorship contribution statement

**Panagiotis Dimas:** Writing – review & editing, Writing – original draft, Visualization, Validation, Supervision, Software, Resources, Project administration, Methodology, Investigation, Funding acquisition, Formal analysis, Data curation, Conceptualization. **Archontia Lykou:** Writing – review & editing, Writing – original draft, Visualization, Validation, Supervision, Software, Resources, Project administration, Methodology, Investigation, Funding acquisition, Formal analysis, Data curation, Conceptualization. **Akis Zarkadoulas:** Writing – review & editing, Writing – original draft, Visualization, Validation, Supervision, Software, Resources, Project administration, Methodology, Investigation, Funding acquisition, Formal analysis, Data curation, Conceptualization. **Georgia-Konstantina Sakki:** Writing – review & editing, Writing – original draft, Visualization, Validation, Supervision, Software, Resources, Project administration, Methodology, Investigation, Funding acquisition, Formal analysis, Data curation, Conceptualization. **Andreas Efstratiadis:** Writing – review & editing, Writing – original draft, Visualization, Validation, Supervision, Software, Resources, Project administration, Methodology, Investigation, Funding acquisition, Formal analysis, Data curation, Conceptualization. **Christos Makropoulos:** Writing – review & editing, Writing – original draft, Visualization, Validation, Supervision, Software, Resources, Project administration, Methodology, Investigation, Funding acquisition, Formal analysis, Data curation, Conceptualization. **Argyro Louloudi:** Writing – review & editing, Writing – original draft, Visualization, Validation, Supervision, Software, Resources, Project administration, Methodology, Investigation, Funding acquisition, Formal analysis, Data curation, Conceptualization.

## Consent to participate

Not applicable, as this study did not involve any human participants as subjects.

## Consent to publish

All authors consent to the publication of this manuscript in the *natural Hazards Journal*, should it be accepted.

## Ethical approval

This study did not involve any human participants or animals as subjects and thus did not require ethical approval.

## Availability of data and materials

The data may be available upon request.

## Funding

Not applicable.

## Declaration of competing interest

The authors declare that they have no known competing financial interests or personal relationships that could have appeared to influence the work reported in this paper.

## Acknowledgements

The research of this paper was performed within the framework of the project titled “Analysis of dam break and flood wave routing across a pumped hydropower storage project at location Sfikia H/P reservoir (Brava)”. The authors would like to express their sincere gratitude to PPC S.A. for their invaluable support and collaboration, which greatly contributed to the successful completion of this study.

## Data availability

No data was used for the research described in the article.

## References

[1] O.A. Adebimpe, D. Proverbs, V.O. Oladokun, Pumped-hydro storage systems and flood risk mitigation: a proposed nexus, International Journal of Environmental Impacts: Management, Mitigation and Recovery 3 (4) (2020) 352–362, https://doi.org/10.2495/EI-V3-N4-352-362.
[2] A.B. Gurung, A. Borsdorf, L. Füreder, F. Kienast, P. Matt, C. Scheidegger, L. Schmocker, M. Zappa, K. Volkart, Rethinking pumped storage hydropower in the European alps, mred 36 (2) (2016) 222–232, https://doi.org/10.1659/MRD-JOURNAL-D-15-00069.1.
[3] J.-F. Zhao, U.-J. Oh, J.-C. Park, E.S. Park, H.-B. Im, K.Y. Lee, J.-S. Choi, A review of world-wide advanced pumped storage hydropower technologies, IFAC-PapersOnLine 55 (9) (2022) 170–174, https://doi.org/10.1016/j.ifacol.2022.07.030.
[4] Z. Dong, J. Tan, E. Muljadi, R.M. Nelms, A. St-Hilaire, M. Pevarnik, M.D. Jacobson, Developing of Quaternary pumped storage hydropower for dynamic studies, IEEE Trans. Sustain. Energy 11 (4) (2020) 2870–2878, https://doi.org/10.1109/TSTE.2020.2980585.
[5] D. Gilfillan, J. Pittock, Pumped storage hydropower for sustainable and low-carbon electricity grids in Pacific rim economies, Energies 15 (9) (2022) 3139, https://doi.org/10.3390/en15093139.
[6] A. Zisos, G.-K. Sakki, A. Efstratiadis, Mixing renewable energy with pumped hydropower storage: design optimization under uncertainty and other challenges, Sustainability 15 (18) (2023) 13313, https://doi.org/10.3390/su151813313.
[7] D. De Wrachien, Dam-Break Problems, Solutions and Case Studies, WIT press, 2009 [place unknown].
[8] J. Kriaučiūnienė, D. Šarauskienė, Uncertainty estimation in the modeling of a flood wave caused by a dam failure in a hydropower system with pumped hydro energy storage, Sustainability 16 (9) (2024) 3528, https://doi.org/10.3390/su16093528.
[9] W. Qiu, Y. Li, L. Wen, Z. Si, Y. Zhang, Y. Duan, Analysis of the galleries cracking causes in the backfill area of pumped storage power station based on monitoring and numerical simulation: a case study of hohhot upper reservoir, Struct. Health Monit. (2024) 14759217241259967, https://doi.org/10.1177/14759217241259967.
[10] B. Zhu, Y. Cao, B. Xia, J. Yan, H. Chen, L. Sun, J. Li, A.G.L. Borthwick, Combined dam-break modes between upper and lower reservoirs of pumped storage hydropower stations and associated flood risk assessment, Water Supply 24 (10) (2024) 3479–3501, https://doi.org/10.2166/ws.2024.223.
[11] B. Guan, J. Hou, J. Lv, D. Li, G. Chen, Y. Fang, L. Shi, Numerical simulation of dam-break flood routing in pumped storage power stations with multi-conditions and disaster impact analysis, Water Resour. Manag. (2024), https://doi.org/10.1007/s11269-024-03987-6 [Internet]. (Accessed 13 January 2025).
[12] A. Harby, J. Sauterleute, M. Korpås, Å. Killingtveit, E. Solvang, T. Nielsen, Pumped storage hydropower, in: Transition to Renewable Energy Systems, John Wiley & Sons, Ltd, 2013, pp. 597–618, https://doi.org/10.1002/9783527673872.ch29 [Internet]. [place unknown]. (Accessed 13 January 2025).
[13] J.I. Pérez-Díaz, M. Chazarra, J. García-González, G. Cavazzini, A. Stoppato, Trends and challenges in the operation of pumped-storage hydropower plants, Renew. Sustain. Energy Rev. 44 (2015) 767–784, https://doi.org/10.1016/j.rser.2015.01.029.
[14] J. Nasir, A. Javed, M. Ali, K. Ullah, S.A.A. Kazmi, Capacity optimization of pumped storage hydropower and its impact on an integrated conventional hydropower plant operation, Appl. Energy 323 (2022) 119561, https://doi.org/10.1016/j.apenergy.2022.119561.
[15] H. Wang, D. Li, T. Sheng, J. Sheng, P. Jing, D. Zhang, A modeling of human reliability analysis on dam failure caused by extreme weather, Appl. Sci. 13 (23) (2023) 12968, https://doi.org/10.3390/app132312968.
[16] W. Ouyang, F. Hao, K. Song, X. Zhang, Cascade dam-induced hydrological disturbance and environmental impact in the upper stream of the yellow river, Water Resour. Manag. 25 (3) (2011) 913–927, https://doi.org/10.1007/s11269-010-9733-6.
[17] G. Pescaroli, D. Alexander, A definition of cascading disasters and cascading effects: going beyond the “toppling dominos” metaphor, Planet@ risk 3 (1) (2015) 58–67.

[18] J.D. Hunt, E. Byers, K. Riahi, S. Langan, Comparison between seasonal pumped-storage and conventional reservoir dams from the water, energy and land nexus perspective, Energy Convers. Manag. 166 (2018) 385–401, https://doi.org/10.1016/j.enconman.2018.04.044.
[19] K. Hewitt, Geomorphic hazards in Mountain environments, in: MOUNTAIN GEOMORPHOLOGY. [place unknown], Routledge, 2004.
[20] G.T. Hancox, M.J. McSaveney, V.R. Manville, T.R. Davies, The October 1999 Mt adams rock avalanche and subsequent landslide dam-break flood and effects in poerua river, westland, New Zealand, N. Z. J. Geol. Geophys. 48 (4) (2005) 683–705, https://doi.org/10.1080/00288306.2005.9515141.
[21] K. Hewitt, Disturbance regime landscapes: mountain drainage systems interrupted by large rockslides, Prog. Phys. Geogr. Earth Environ. 30 (3) (2006) 365–393, https://doi.org/10.1191/0309133306pp486ra.
[22] O. Korup, F. Tweed, Ice, moraine, and landslide dams in mountainous terrain, Quat. Sci. Rev. 26 (25) (2007) 3406–3422, https://doi.org/10.1016/j.quascirev.2007.10.012.
[23] O. Korup, J.J. Clague, Natural hazards, extreme events, and Mountain topography, Quat. Sci. Rev. 28 (11) (2009) 977–990, https://doi.org/10.1016/j.quascirev.2009.02.021.
[24] R. Neupane, H. Chen, C. Cao, Review of moraine dam failure mechanism, Geomat. Nat. Hazards Risk 10 (1) (2019) 1948–1966, https://doi.org/10.1080/19475705.2019.1652210.
[25] F.M. Evers, V. Heller, H. Fuchs, W.H. Hager, R. Boes, Landslide-generated impulse waves in reservoirs: basics and computation, VAW-Mitteilungen 254 (2019), https://doi.org/10.3929/ethz-b-000413216 [Internet]. (Accessed 13 January 2025).
[26] Y. Moustakis, S.M. Papalexiou, C.J. Onof, A. Paschalis, Seasonality, intensity, and duration of rainfall extremes change in a warmer climate, Earths Future 9 (3) (2021) e2020EF001824, https://doi.org/10.1029/2020EF001824.
[27] D. Zhong, Y. Sun, M. Li, Dam break threshold value and risk probability assessment for an Earth dam, Nat. Hazards 59 (1) (2011) 129–147, https://doi.org/10.1007/s11069-011-9743-6.
[28] S.J. Peter, A. Siviglia, J. Nagel, S. Marelli, R.M. Boes, D. Vetsch, B. Sudret, Development of probabilistic dam breach model using bayesian inference, Water Resour. Res. 54 (7) (2018) 4376–4400, https://doi.org/10.1029/2017WR021176.
[29] Samuel J. Peter, D.F. Vetsch, A. Siviglia, R. Boes, Probabilistische dammbruchanalyse, Wasser, Energ. Luft 2018 (3) (2018) 179–185.
[30] C.W. Tsai, J.-J. Yeh, C.-H. Huang, Development of probabilistic inundation mapping for dam failure induced floods, Stoch. Environ. Res. Risk Assess. 33 (1) (2019) 91–110, https://doi.org/10.1007/s00477-018-1636-8.
[31] S. Sarchani, A.G. Koutroulis, Probabilistic dam breach flood modeling: the case of valsamiotis dam in Crete, Nat. Hazards 114 (2) (2022) 1763–1814, https://doi.org/10.1007/s11069-022-05446-0.
[32] C. Rizzo, A. Maranzoni, M. D'Oria, Probabilistic mapping and sensitivity assessment of dam-break flood hazard, Hydrol. Sci. J. 68 (5) (2023) 700–718, https://doi.org/10.1080/02626667.2023.2174026.
[33] Z. Cao, W. Huang, G. Pender, X. Liu, Even more destructive: cascade dam break floods, Journal of Flood Risk Management 7 (4) (2014) 357–373, https://doi.org/10.1111/jfr3.12051.
[34] M. Elkholy, L.A. LaRocque, M.H. Chaudhry, J. Imran, Experimental investigations of partial-breach dam-break flows, J. Hydraul. Eng. 142 (11) (2016) 04016042, https://doi.org/10.1061/(ASCE)HY.1943-7900.0001185.
[35] J. Říha, S. Kotaška, L. Petrula, Dam break modeling in a Cascade of small earthen dams: case study of the Čižina river in the Czech Republic, Water 12 (8) (2020) 2309, https://doi.org/10.3390/w12082309.
[36] A. Zweifel, W.H. Hager, H.-E. Minor, Plane impulse waves in reservoirs, J. Waterw. Port, Coast. Ocean Eng. 132 (5) (2006) 358–368, https://doi.org/10.1061/(ASCE)0733-950X(2006)132:5(358.
[37] V. Heller, W.H. Hager, H.-E. Minor, Landslide generated impulse waves in reservoirs: basics and computation, VAW-Mitteilungen 211 (2009).
[38] H. Fuchs, F.M. Evers, R. Boes, Impulse waves in reservoirs: recent research at VAW, in: E-proceedings of the Hydro 2016 Conference" Achievements, Opportunities and Challenges". [place unknown]: Hydropower and Dams, Aqua-Media International, 2016, pp. 5–7.
[39] B. Huang, Y. Yin, C. Du, Risk management study on impulse waves generated by hongyanzi landslide in three gorges reservoir of China on June 24, 2015, Landslides 13 (3) (2016) 603–616, https://doi.org/10.1007/s10346-016-0702-x.
[40] B. Huang, S.C. Wang, Y.B. Zhao, Impulse waves in reservoirs generated by landslides into shallow water, Coast. Eng. 123 (2017) 52–61, https://doi.org/10.1016/j.coastaleng.2017.03.003.
[41] W.H. Hager, F.M. Evers, Impulse waves in reservoirs: research up to 1990, J. Hydraul. Eng. 146 (10) (2020) 03120002, https://doi.org/10.1061/(ASCE)HY.1943-7900.0001770.
[42] L. Han, P. Wang, P. Mu, Q. Ren, Y. Liu, Experimental investigation of propagation and run-up of rockslide- generated impulse waves in a curved Mountain reservoir, Nat. Hazards 111 (2) (2022) 1375–1399, https://doi.org/10.1007/s11069-021-05099-5.
[43] L. Peyras, C. Carvajal, H. Felix, C. Bacconnet, P. Royet, J.-P. Becue, D. Boissier, Probability-based assessment of dam safety using combined risk analysis and reliability methods – application to hazards studies, European Journal of Environmental and Civil Engineering 16 (7) (2012) 795–817, https://doi.org/10.1080/19648189.2012.672200.
[44] Y. Zhu, X. Niu, J. Wang, C. Gu, Q. Sun, B. Li, L. Huang, A risk assessment model for dam combining the probabilistic and the nonprobabilistic methods, Math. Probl Eng. 2020 (1) (2020) 9518369, https://doi.org/10.1155/2020/9518369.
[45] M. D'Oria, A. Maranzoni, C. Rizzo, Probabilistic flood risk associated with dam-break [internet] [place unknown]: ITA; [accessed 2025 Jan 13], https://air.unipr.it/handle/11381/2937977, 2022.
[46] A. EL Bilali, I. Taleb, A. Nafii, A. Taleb, A practical probabilistic approach for simulating life loss in an urban area associated with a dam-break flood, Int. J. Disaster Risk Reduct. 76 (2022) 103011, https://doi.org/10.1016/j.ijdrr.2022.103011.
[47] H. Ersoy, M. Karahan, K. Gelişli, A. Akgün, T. Anılan, M.O. Sünnetci, B.K. Yahşi, Modelling of the landslide-induced impulse waves in the Artvin dam reservoir by empirical approach and 3D numerical simulation, Eng. Geol. 249 (2019) 112–128, https://doi.org/10.1016/j.enggeo.2018.12.025.
[48] J. Tan, B. Huang, Y. Zhao, Pressure characteristics of landslide-generated impulse waves, J. Mt. Sci. 16 (8) (2019) 1774–1787, https://doi.org/10.1007/s11629-018-5307-5.
[49] M. Bilal, A. Xing, Y. Zhuang, Y. Zhang, K. Jin, Y. Zhu, Y. Leng, Coupled 3D numerical model for a landslide-induced impulse water wave: a case study of the fuquan landslide, Eng. Geol. 290 (2021) 106209, https://doi.org/10.1016/j.enggeo.2021.106209.
[50] H. Wu, Q. Zhong, Z. Deng, Y. Shan, K. Zhao, Numerical investigation of the effect of landslide relative density on the impulse wave amplitude, Ocean Eng. 309 (2024) 118563, https://doi.org/10.1016/j.oceaneng.2024.118563.
[51] Y. Hua, G. Ma, G. Yang, Studies on cooperative emergency regulation of over-level floods of Cascade reservoirs, MATEC Web Conf. 246 (2018) 01122, https://doi.org/10.1051/matecconf/201824601122.
[52] J. Chen, P. Zhong, M. Wang, F. Zhu, X. Wan, Y. Zhang, A risk-based model for real-time flood control operation of a Cascade reservoir system under emergency conditions, Water 10 (2) (2018) 167, https://doi.org/10.3390/w10020167.
[53] Y. Jiang, R. Zhang, B. Wang, Scenario-based approach for emergency operational response: implications for reservoir management decisions, Int. J. Disaster Risk Reduct. 80 (2022) 103192, https://doi.org/10.1016/j.ijdrr.2022.103192.
[54] A.B. De Almeida, A.B. Franco, Modeling of dam-break flow, in: M.H. Chaudhry, L.W. Mays (Eds.), Computer Modeling of Free-Surface and Pressurized Flows, Springer Netherlands, Dordrecht, 1994, pp. 343–373, https://doi.org/10.1007/978-94-011-0964-2_12 [Internet]. (Accessed 13 January 2025).
[55] W. Wu, S.S. Wang, One-dimensional modeling of dam-break flow over movable beds, J. Hydraul. Eng. 133 (1) (2007) 48–58, https://doi.org/10.1061/(ASCE)0733-9429(2007)133:1(48.
[56] M. Pilotti, A. Maranzoni, L. Milanesi, M. Tomirotti, G. Valerio, Dam-break modeling in alpine valleys, J. Mt. Sci. 11 (6) (2014) 1429–1441, https://doi.org/10.1007/s11629-014-3042-0.
[57] O. Seyedashraf, M. Mehrabi, A.A. Akhtari, Novel approach for dam break flow modeling using computational intelligence, J. Hydrol. 559 (2018) 1028–1038, https://doi.org/10.1016/j.jhydrol.2018.03.001.

[58] F. Aureli, A. Maranzoni, G. Petaccia, Review of historical dam-break events and laboratory tests on real topography for the validation of numerical models, Water 13 (14) (2021) 1968, https://doi.org/10.3390/w13141968.
[59] Z. Chen, L. Wang, X. Zhou, S. Chen, Improvement to the analytical method for dam breach flood evaluation, in: J.-M. Zhang, L. Zhang, R. Wang (Eds.), Dam Breach Modelling and Risk Disposal, Springer International Publishing, Cham, 2020, pp. 3–23, https://doi.org/10.1007/978-3-030-46351-9_1.
[60] H. Wang, Y. Zhou, S. Wang, F. Wang, Coupled model constructed to simulate the landslide dam flood discharge: a case study of baige landslide dam, jinsha river, Front. Earth Sci. 14 (1) (2020) 63–76, https://doi.org/10.1007/s11707-019-0805-5.
[61] J. Ma, F. Zhou, C. Yue, Q. Sun, X. Wang, The coupled application of the DB-IWHR model and the MIKE 21 model for the assessment of dam failure risk, Water 16 (20) (2024) 2919, https://doi.org/10.3390/w16202919.
[62] Y. Xiong, A dam break analysis using HEC-RAS, J. Water Resour. Protect. 3 (6) (2011) 370–379, https://doi.org/10.4236/jwarp.2011.36047.
[63] S. Kilania, B.R. Chahar, A dam break analysis using HEC-RAS, 382–389, https://doi.org/10.1061/9780784482353.036, 2019.
[64] A. Raman, F. Liu, An investigation of the brumadinho dam break with HEC RAS simulation [Internet], https://doi.org/10.48550/arXiv.1911.05219, 2019. (Accessed 13 January 2025).
[65] M. Pilotti, L. Milanesi, V. Bacchi, M. Tomirotti, A. Maranzoni, Dam-break wave propagation in alpine valley with HEC-RAS 2D: experimental cancano test case, J. Hydraul. Eng. 146 (6) (2020) 05020003, https://doi.org/10.1061/(ASCE)HY.1943-7900.0001779.
[66] A. Bharath, A.V. Shivapur, C.G. Hiremath, R. Maddamsetty, Dam break analysis using HEC-RAS and HEC-GeoRAS: a case study of hidkal dam, Karnataka state, India, Environ. Chall. 5 (2021) 100401, https://doi.org/10.1016/j.envc.2021.100401.
[67] N.D. Katopodes, T. Strelkoff, Two-dimensional shallow water-wave models, J. Eng. Mech. Div. 105 (2) (1979) 317–334, https://doi.org/10.1061/JMCEA3.0002468.
[68] V. Casulli, Semi-implicit finite difference methods for the two-dimensional shallow water equations, J. Comput. Phys. 86 (1) (1990) 56–74, https://doi.org/10.1016/0021-9991(90)90091-E.
[69] T.H. Yoon, S.-K. Kang, Finite volume model for two-dimensional shallow water flows on unstructured grids, J. Hydraul. Eng. 130 (7) (2004) 678–688, https://doi.org/10.1061/(ASCE)0733-9429(2004)130:7(678.
[70] P.-W. Li, C.-M. Fan, Generalized finite difference method for two-dimensional shallow water equations, Eng. Anal. Bound. Elem. 80 (2017) 58–71, https://doi.org/10.1016/j.enganabound.2017.03.012.
[71] D. Hizume, T. Tabata, K. Hiramatsu, M. Harada, A. Ozaki, Hydraulic analyses using two-dimensional shallow water equations for functional evaluation of the yamadazeki barrage in the chikugo river, Japan, Paddy Water Environ. 22 (1) (2024) 109–123, https://doi.org/10.1007/s10333-023-00956-4.
[72] D. Hu, Z. Chen, Z. Li, Y. Zhu, An implicit 1D-2D deeply coupled hydrodynamic model for shallow water flows, J. Hydrol. 631 (2024) 130833, https://doi.org/10.1016/j.jhydrol.2024.130833.
[73] P. Jing, J. Sheng, T. Hu, K. Dong, L. Guo, R. Zhu, Y. Liu, Y. Huang, X. Xu, Revealing the stability evolution of the hydropower megaproject system based on the emergy ecological network model, ACS EST Water. 5 (4) (2025) 1789–1802, https://doi.org/10.1021/acsestwater.4c01162.
[74] M. Azmi, K. Thomson, Dam breach parameters: from data-driven-based estimates to 2-dimensional modeling, Nat. Hazards 120 (5) (2024) 4423–4461, https://doi.org/10.1007/s11069-023-06382-3.
[75] H.O. Marangoz, T. Anılan, S. Karasu, Investigating the non-linear effects of breach parameters on a dam break study, Water Resour. Manag. 38 (5) (2024) 1773–1790, https://doi.org/10.1007/s11269-024-03765-4.
[76] T. Dezert, F.G. Sigtryggsdóttir, Evaluation of parametric breach models from prototype and historical embankment dams under overtopping conditions, J. Geotech. Geoenviron. Eng. 150 (4) (2024) 04024015, https://doi.org/10.1061/JGGEFK.GTENG-12128.
[77] N. Silva-Cancino, F. Salazar, E. Bladé, M. Sanz-Ramos, Influence of breach parameter models on hazard classification of off-stream reservoirs, Water Sci. Eng. (2024), https://doi.org/10.1016/j.wse.2024.05.001 [Internet]. (Accessed 13 January 2025).
[78] P.D.P.O. Peramuna, N.G.P.B. Neluwala, K.K. Wijesundara, S. Venkatesan, S. De Silva, P.B.R. Dissanayake, Novel approach to the derivation of dam breach parameters in 2D hydrodynamic modeling of earthquake induced dam failures, Sci. Total Environ. 927 (2024) 171505, https://doi.org/10.1016/j.scitotenv.2024.171505.
[79] D.L. Fread, BREACH, an erosion model for earthen dam failures. [place unknown]: Hydrologic Research Laboratory, National Weather Service, NOAA MD, United States, 1988.
[80] S.J. Park, K.Y. Han, H.G. Choi, Flood routing of sequential failure of dams by numerical model, KSCE Journal of Civil and Environmental Engineering Research 33 (5) (2013) 1797–1807.
[81] G.B. Crosta, S. Imposimato, D. Roddeman, Landslide spreading, impulse water waves and modelling of the vajont rockslide, Rock Mech. Rock Eng. 49 (6) (2016) 2413–2436, https://doi.org/10.1007/s00603-015-0769-z.
[82] A. Franci, M. Cremonesi, U. Perego, G. Crosta, E. Oñate, 3D simulation of vajont disaster. Part 1: numerical formulation and validation, Eng. Geol. 279 (2020) 105854, https://doi.org/10.1016/j.enggeo.2020.105854.
[83] A. Franci, M. Cremonesi, U. Perego, E. Oñate, G. Crosta, 3D simulation of vajont disaster. Part 2: multi-Failure scenarios, Eng. Geol. 279 (2020) 105856, https://doi.org/10.1016/j.enggeo.2020.105856.
[84] S. Chen, Q. Zhong, G. Shen, Numerical modeling of earthen dam breach due to piping failure, Water Sci. Eng. 12 (3) (2019) 169–178, https://doi.org/10.1016/j.wse.2019.08.001.
[85] W. Ma, G. Zhang, Y. Yang, P. Wang, Y. Zhao, Q. Lin, The piping failure mechanism of a loess dam: the 2021 dam break of the yang village reservoir in China, Front. Earth Sci. 10 (2022), https://doi.org/10.3389/feart.2022.892179 [Internet]. (Accessed 13 January 2025).
[86] L. Nibbi, P. Sospiro, M. De Lucia, C.-C. Wu, Improving pumped hydro storage flexibility in China: scenarios for advanced solutions adoption and policy recommendations, Energies 15 (21) (2022) 7918, https://doi.org/10.3390/en15217918.
[87] R. Wang, W. Yang, Y. Huang, X. Li, Y. Liu, J. Chen, Q. Cheng, Y. Mei, Y. Cheng, P. Liu, Coordinating regulation reliability and quality of pumped storage units for renewables by a novel scheduling-control synergic model, Appl. Energy 376 (2024) 124162, https://doi.org/10.1016/j.apenergy.2024.124162.
[88] K. Dong, D. Yang, J. Sheng, W. Zhang, P. Jing, Dynamic planning method of evacuation route in dam-break flood scenario based on the ACO-GA hybrid algorithm, Int. J. Disaster Risk Reduct. 100 (2024) 104219, https://doi.org/10.1016/j.ijdrr.2023.104219.
[89] I. Kitowski, A. Sujak, M. Drygaś, The water dimensions of Russian – ukrainian conflict, Ecohydrol. Hydrobiol. 23 (3) (2023) 335–345, https://doi.org/10.1016/j.ecohyd.2023.05.001.
[90] G.W. Brunner, Using HEC-RAS for dam break studies, in: Training Document No. 39, 2014.
[91] J.E. Costa, Floods from Dam Failures, US Geological Survey, 1985 [place unknown].
[92] T.A. Atallah, A Review on Dams and Breach Parameters Estimation, 2002.
[93] C. Ntemiroglou, G.-K. Sakki, A. Efstratiadis, Flood control across hydropower dams: the value of safety, in: Role of Dams and Reservoirs in a Successful Energy Transition, CRC Press, 2023 [place unknown].
[94] J.D. Rogers, C.M. Watkins, J.-W. Chung, The 2005 upper taum sauk dam failure: a case history, Environ. Eng. Geosci. 16 (3) (2010) 257–289, https://doi.org/10.2113/gseegeosci.16.3.257.
[95] S. Mei, Q. Zhong, M. Yang, S. Chen, Y. Shan, L. Zhang, Overtopping-induced breaching process of concrete-faced rockfill dam: a case study of upper taum sauk dam, Eng. Fail. Anal. 144 (2023) 106982, https://doi.org/10.1016/j.engfailanal.2022.106982.
[96] A.C.-U. Okeke, F. Wang, Hydromechanical constraints on piping failure of landslide dams: an experimental investigation, Geoenviron Disasters 3 (1) (2016) 4, https://doi.org/10.1186/s40677-016-0038-9.
[97] D.C. Froehlich, Embankment dam breach parameters revisited, in: Proc Conference on Water Resources Engineering, San Antonio, Texas, 1995, ASCE, 1995 [place unknown].
[98] D.C. Froehlich, Embankment dam breach parameters and their uncertainties, J. Hydraul. Eng. 134 (12) (2008) 1708–1721, https://doi.org/10.1061/(ASCE)0733-9429(2008)134:121708.

[99] T.C. MacDonald, J. Langridge-Monopolis, Breaching charateristics of dam failures, J. Hydraul. Eng. 110 (5) (1984) 567–586, https://doi.org/10.1061/(ASCE)0733-9429(1984)110:5567.
[100] J.L. Von Thun, D.R. Gillette, Guidance on breach parameters. [place unknown]: US Department of the Interior, Bureau of Reclamation, 1990.
[101] Y. Xu, L.M. Zhang, Breaching parameters for Earth and rockfill dams, J. Geotech. Geoenviron. Eng. 135 (12) (2009) 1957–1970, https://doi.org/10.1061/(ASCE)GT.1943-5606.0000162.
[102] L. Vonwiller, D. Vetsch, S. Peter, R. Boes, Methode zur Beurteilung des maximalen Breschenabflusses bei progressivem Bruch homogener Erdschüttdämme an kleinen Stauhaltungen, Wasser, Energ. Luft 107 (1) (2015) 37–43.
[103] D.F. Vetsch, R. Boes, Vereinfachte Modellierung des progressiven Bruchs bei kleinen Erdschüttdämmen, Wasserwirtschaft 106 (6) (2016) 140–143.
[104] F. Macchione, Model for predicting floods due to earthen dam breaching. I: formulation and evaluation, J. Hydraul. Eng. 134 (12) (2008) 1688–1696, https://doi.org/10.1061/(ASCE)0733-9429(2008)134:121688.
[105] S.J. Peter, Dam Break Analysis Under Uncertainy, 2017.
[106] I. Shustikova, A. Domeneghetti, J.C. Neal, P. Bates, A. Castellarin, Comparing 2D capabilities of HEC-RAS and LISFLOOD-FP on complex topography, Hydrol. Sci. J. 64 (14) (2019) 1769–1782, https://doi.org/10.1080/02626667.2019.1671982.
[107] C.A. De Moura, C.S. Kubrusly, The courant–friedrichs–lewy (cfl) condition, Adv. Math. Commun. 10 (12) (2013) 45–90.
[108] V. Te Chow, Open Channel Hydraulics, 1959 [place unknown].
[109] A.S. Alzahrani, Application of Two-Dimensional Hydraulic Modeling in Riverine Systems Using HEC-RAS [Internet]. [place unknown], University of Dayton, 2017 [accessed 2025 Jan 15], https://etd.ohiolink.edu/acprod/odb_etd/etd/r/1501/10?clear=10&p10_accession_num=dayton1493135117254329.
[110] A. Efstratiadis, I. Tsoukalas, D. Koutsoyiannis, Generalized storage-reliability-yield framework for hydroelectric reservoirs, Hydrol. Sci. J. 66 (4) (2021) 580–599, https://doi.org/10.1080/02626667.2021.1886299.
[111] J.A. Roberson, J.J. Cassidy, M.H. Chaudhry, Hydraulic engineering. [place unknown], John Wiley & Sons, 1998.
[112] A. Efstratiadis, Lecture notes on hydraulic structures and dams [internet] [accessed 2025 Jan 15], https://www.itia.ntua.gr/en/docinfo/2435/, 2023.
[113] G.W. Brunner, HEC-RAS river analysis system. Hydraulic Reference Manual, 1997, Version 1.0.
[114] J.J. Monaghan, A. Kos, Scott Russell's wave generator, Phys. Fluids 12 (3) (2000) 622–630, https://doi.org/10.1063/1.870269.
[115] M. Di Risio, P. Sammarco, Analytical modeling of landslide-generated waves, J. Waterw. Port, Coast. Ocean Eng. 134 (1) (2008) 53–60, https://doi.org/10.1061/(ASCE)0733-950X(2008)134:153.
[116] M. Abramowitz, I.A. Stegun, Handbook of Mathematical Functions with Formulas, Graphs, and Mathematical Tables, US Government printing office, 1948 [place unknown].
[117] R. Soulsby, Dynamics of marine sands: a manual for practical applications, Oceanogr. Lit. Rev. 9 (44) (1997) 947.
[118] Y. Goda, Random seas and design of maritime structures, World scientific (2010) [place unknown].
[119] V. Nguyen-Tien, R.J.R. Elliott, E.A. Strobl, Hydropower generation, flood control and dam cascades: a national assessment for Vietnam, J. Hydrol. 560 (2018) 109–126, https://doi.org/10.1016/j.jhydrol.2018.02.063.
[120] E. Dimitriou, A. Efstratiadis, I. Zotou, A. Papadopoulos, T. Iliopoulou, G.-K. Sakki, K. Mazi, E. Rozos, A. Koukouvinos, A.D. Koussis, et al., Post-analysis of daniel extreme flood event in Thessaly, Central Greece: practical lessons and the value of state-of-the-art water-monitoring networks, Water 16 (7) (2024) 980, https://doi.org/10.3390/w16070980.
[121] T. Iliopoulou, N. Malamos, D. Koutsoyiannis, Regional Ombrian curves: design rainfall estimation for a spatially diverse rainfall regime, Hydrology 9 (5) (2022) 67, https://doi.org/10.3390/hydrology9050067.
[122] M.R. Rahmanian, M.A. Banihashemi, Sediment distribution pattern in some Iranian dams based on a new empirical reservoir shape function, Lake Reserv. Manag. 27 (3) (2011) 245–255, https://doi.org/10.1080/07438141.2011.602510.
[123] B. Michalec, Evaluation of an empirical reservoir shape function to define sediment distributions in small reservoirs, Water 7 (8) (2015) 4409–4426, https://doi.org/10.3390/w7084409.
[124] D.C. Froehlich, Peak outflow from breached embankment dam, J. Water Resour. Plann. Manag. 121 (1) (1995) 90–97.
[125] SCS, e. Simplified Dam-Breach Routing Procedur, 1981.
[126] V.K. Hagen, Re-evaluation of Design Floods and Dam Safety, 1982.
[127] K.P. Singh, A. Snorrason, Sensitivity of outflow peaks and flood stages to the selection of dam breach parameters and simulation models, J. Hydrol. 68 (1) (1984) 295–310, https://doi.org/10.1016/0022-1694(84)90217-8.
[128] S.G. Evans, The maximum discharge of outburst floods caused by the breaching of man-made and natural dams, Can. Geotech. J. 23 (3) (1986) 385–387, https://doi.org/10.1139/t86-053.
[129] Institut de Mécanique des Fluides de Toulouse, -9. Rapport No 328, 1977.
[130] D.D. Meringolo, F. Aristodemo, S. Servidio, P.G.F. Filianoti, Large eddy simulations of turbulence diffusion within the smoothed particle hydrodynamics, Phys. Fluids 36 (4) (2024) 045105, https://doi.org/10.1063/5.0202974.
[131] Q. Kriaa, S. Viroulet, L. Lacaze, Modeling of impulse waves generated by a viscous collapse in water, Phys Rev Fluids 7 (5) (2022) 054801, https://doi.org/10.1103/PhysRevFluids.7.054801.
[132] K. Sakai, Wave propagation In/On liquids and spectroscopy of viscoelasticity and surface tension, in: Ultrasonics: Physics and Applications [Internet], IOP Publishing, 2022, https://doi.org/10.1088/978-0-7503-4936-9ch2 [place unknown]. (Accessed 21 January 2025).
[133] L. Han, P. Wang, T. Yu, Wave types and energy conversion of impulse waves generated by landslides into Mountain reservoirs, Sci. Rep. 12 (1) (2022) 4035, https://doi.org/10.1038/s41598-022-07993-9.
[134] Y. Goda, Dynamic response of upright breakwaters to impulsive breaking wave forces, Coast. Eng. 22 (1) (1994) 135–158, https://doi.org/10.1016/0378-3839(94)90051-5.
[135] T. Cao, P. Wang, Z. Qiu, J. Ren, Influence of impulse waves generated by rocky landslides on the pressure exerted on bank slopes, J. Mt. Sci. 18 (5) (2021) 1159–1176, https://doi.org/10.1007/s11629-020-6076-5.
[136] S. Wang, B. le Mehaute, C.-C. Lu, Effect of dispersion on impulsive waves, Mar. Geophys. Res. 9 (1) (1987) 95–111, https://doi.org/10.1007/BF00338252.
[137] Y. Shen, X. Yin, Analysis of geometric dispersion effect of impact-induced transient waves in composite rod using dynamic substructure method, Appl. Math. Model. 40 (3) (2016) 1972–1988, https://doi.org/10.1016/j.apm.2015.09.022.
[138] S.A. Mattis, C.E. Kees, M.V. Wei, A. Dimakopoulos, C.N. Dawson, Computational model for wave attenuation by flexible vegetation, J. Waterw. Port, Coast. Ocean Eng. 145 (1) (2019) 04018033, https://doi.org/10.1061/(ASCE)WW.1943-5460.0000487.
[139] T.J. van Veelen, T.P. Fairchild, D.E. Reeve, H. Karunarathna, Experimental study on vegetation flexibility as control parameter for wave damping and velocity structure, Coast. Eng. 157 (2020) 103648, https://doi.org/10.1016/j.coastaleng.2020.103648.
[140] H. Xie, J. Lyu, Y. Bao, Y. Yu, Y. Li, X. Zheng, X. He, Spatial and temporal variation of nearshore significant wave height in the three gorges reservoir, China, Ecol. Indic. 151 (2023) 110343, https://doi.org/10.1016/j.ecolind.2023.110343.
[141] X. Zhou (周昔东), L. Su (苏立君), H. Yuan (袁浩), Y. Mao (毛云飞), Q. Sun (孙倩), Experimental study on the influence of water depth and bed slope variations on dam-break flood wave propagation, Phys. Fluids 36 (7) (2024) 075133, https://doi.org/10.1063/5.0219430.
[142] J. Li, Z. Cao, Q. Liu, Waves and sediment transport due to granular landslides impacting reservoirs, Water Resour. Res. 55 (1) (2019) 495–518, https://doi.org/10.1029/2018WR023191.
[143] S.I. de Lange, N. Santa, S.P. Pudasaini, M.G. Kleinhans, T. de Haas, Debris-flow generated tsunamis and their dependence on debris-flow dynamics, Coast. Eng. 157 (2020) 103623, https://doi.org/10.1016/j.coastaleng.2019.103623.
[144] M. Quecedo, M. Pastor, M.I. Herreros, Numerical modelling of impulse wave generated by fast landslides, Int. J. Numer. Methods Eng. 59 (12) (2004) 1633–1656, https://doi.org/10.1002/nme.934.
[145] M. Rauter, L. Hoße, R.P. Mulligan, W.A. Take, F. Løvholt, Numerical simulation of impulse wave generation by idealized landslides with OpenFOAM, Coast. Eng. 165 (2021) 103815, https://doi.org/10.1016/j.coastaleng.2020.103815.